

Microgranitic Enclaves as Products of Self-mixing Events: a Study of Open-system Processes in the Mauá Granite, São Paulo, Brazil, Based on *in situ* Isotopic and Trace Elements in Plagioclase

ADRIANA ALVES^{1*}, VALDECIR DE ASSIS JANASI¹,
ANTONIO SIMONETTI^{2†} AND LARRY HEAMAN²

¹INSTITUTO DE GEOCIÊNCIAS, RUA DO LAGO, 562, UNIVERSITY OF SÃO PAULO, SÃO PAULO, 05508-080, BRAZIL

²DEPARTMENT OF EARTH AND ATMOSPHERIC SCIENCES, 1–26 EARTH SCIENCES BUILDING, UNIVERSITY OF ALBERTA, EDMONTON, ALBERTA, T6G 2E3, CANADA

RECEIVED MARCH 20, 2009; ACCEPTED OCTOBER 15, 2009

Felsic microgranular enclaves with structures indicating that they interacted in a plastic state with their chemically similar host granite are abundant in the Mauá Pluton, SE Brazil. Larger plagioclase xenocrysts are in textural disequilibrium with the enclave groundmass and show complex zoning patterns with partially resorbed An-rich cores (locally with patchy textures) surrounded by more sodic rims. In situ laser ablation–(multi-collector) inductively coupled plasma mass spectrometry trace element and Sr isotopic analyses performed on the plagioclase xenocrysts indicate open-system crystallization; however, no evidence of derivation from more primitive basic melts is observed. The An-rich cores have more radiogenic initial Sr isotopic ratios that decrease towards the outermost part of the rims, which are in isotopic equilibrium with the matrix plagioclase. These profiles may have been produced by either (1) diffusional re-equilibration after rim crystallization from the enclave-forming magma, as indicated by relatively short calculated residence times, or (2) episodic contamination with a decrease of the contaminant ratio proportional to the extent to which the country rocks were isolated by the crystallization front. Profiles of trace elements with high diffusion coefficients would require unrealistically long residence times, and can be modeled in terms of fractional crystallization. A combination of trace element and Sr isotope data suggests that the felsic microgranular enclaves from the Mauá Pluton are the products of interaction between end-member magmas that had similar compositions, thus recording ‘self-mixing’ events.

KEY WORDS: *felsic microgranular enclaves; granite; plagioclase xenocryst; Rb–Sr isotopes; trace element*

INTRODUCTION

Progress in understanding the evolution of granitic magmas and the dynamics of magma chambers has benefited significantly from the study of enclaves, particularly since the widespread recognition that most mafic microgranular enclaves correspond to blobs of new magma that intruded and were trapped in the host granite (Didier, 1973; Wiebe, 1974; Vernon, 1984; Frost & Mahood, 1987; Didier & Barbarin, 1991). Felsic microgranular enclaves also appear to be common, although they have been much less studied than their mafic and intermediate equivalents (e.g. Donaire *et al.*, 2005; Waight *et al.*, 2007; Wiebe *et al.*, 2007), and may show very similar field relations indicative of injection into a colder granitic crystal–melt ‘mush’. Because the enclaves have a similar composition to the host granite magma, mixing is expected to result in petrographically similar products; thus the volume of enclave-generating magma intruding the host magma may be higher than deduced from field inspection. However, there has been comparatively little research focused on felsic microgranular enclaves, in part because

*Corresponding author. Telephone: +55 (11) 3091-4023. Fax: +55 (11) 3091-4258. E-mail: adrianaalves@usp.br

†Present address: Department of Civil Engineering and Geological Sciences, 156 Fitzpatrick Hall, University of Notre Dame, Notre Dame, IN 46556, USA.

© The Author 2009. Published by Oxford University Press. All rights reserved. For Permissions, please e-mail: journals.permissions@oxfordjournals.org

they often have a dark color resulting from their fine grain size and may therefore be difficult to distinguish from the more mafic enclaves. In addition, some felsic enclaves are thought to be produced by protracted hybridization processes; therefore such inclusions provide less information on the original magma composition.

As consistently demonstrated by recent studies (Davidson & Tepley, 1997; Waight *et al.*, 2000, 2001; Davidson *et al.*, 2001; Gagnevin *et al.*, 2005), isotope heterogeneity at the mineral scale is very common in volcanic and plutonic rocks of varied compositions. This allows for open-system assimilation–crystal fractionation (AFC) processes to be identified and quantified in terms of endmembers and products; in favorable cases, the timescale of the process can also be estimated (for reviews, see Davidson *et al.*, 2007; Costa *et al.*, 2008).

The Mauá Granite is one of several granitoid intrusions in SE Brazil in which felsic microgranular enclaves are abundant, and where evidence for the intrusion of coeval basic magmas is absent. In this study, we attempt to determine the origin and mode of formation of these enclaves, and their bearing on the evolution of the magma chamber. For this purpose, we conducted a detailed field, petrographic, geochemical, and Sr isotopic investigation on both enclaves and their host granite. In particular, we used the chemical and isotopic zoning of feldspar ‘phenocrysts’ as a tool to unravel open-system contamination processes in melt evolution and provide important constraints on the generation mechanisms of felsic microgranular enclaves.

THE MAUÁ PLUTON

Geology

The Mauá Granite is one of a series of granitic plutons and batholiths of Neoproterozoic age (mostly 650–590 Ma) intruding the Embu Domain in the central portion of the Ribeira Fold Belt, Brazil (e.g. Janasi *et al.*, 2003). The Embu Domain is locally dominated by low- to medium-grade pelitic schists locally containing the assemblage muscovite + biotite + garnet ± kyanite ± sillimanite. Scattered windows of Paleoproterozoic basement are composed of migmatitic orthogneiss. Most of the granite plutons from this portion of the Ribeira Fold Belt exhibit a well-developed foliation related to syn-orogenic emplacement and appear to be slightly older than the Mauá pluton. Hornblende-bearing, typically metaluminous granites are lacking within these plutons, which are compositionally varied from less fractionated porphyritic biotite granites to equigranular two-mica (±garnet, tourmaline) granites and minor (±muscovite ±garnet) tourmaline aplites–pegmatites.

The Mauá pluton is an elongate body oriented N45E (22 km × 2–2.5 km; *c.* 45 km², Fig. 1) intruding low- to medium-grade metasedimentary rocks and has been

dated at 588 ± 2 Ma [U–Pb in monazite; isotope dilution thermal ionization mass spectrometry (ID-TIMS); Filipov & Janasi, 2001]. It largely comprises grey porphyritic biotite monzogranites that appear to evolve gradually to a small cupola of muscovite leucogranite located at its southwestern end, with an intermediate zone of inequigranular biotite monzogranite.

The porphyritic biotite monzogranites have a colour index (CI) ranging from 6 to 8.4 and contain 1–3 cm long alkali feldspar megacrysts. These rocks host various types of enclave of which the most abundant are ellipsoidal decimetre-sized microgranitic enclaves; less common are elongated biotite–K-feldspar-rich (‘schistose’) enclaves, schlieren and gneissic xenoliths. The inequigranular biotite monzogranite (CI 4–6) contains scarce primary muscovite, reflecting its slightly peraluminous character, and both monazite and allanite as light rare earth element (LREE)-bearing accessory minerals. Plagioclase is sodic oligoclase (An 10–28) with both normal and oscillatory zoning. Muscovite leucogranite is restricted to a cupola zone at the SW termination of the pluton, and has a panxenomorphic texture, CI < 4, and lower contents of biotite and plagioclase (An < 8) but higher modal alkali feldspar. Accessory minerals are scarce and include monazite, apatite, and tourmaline.

Structures

Flowage, banding and pipe-vortex structures

The porphyritic granite contains abundant structures generated by flow of early crystallized material. Among the most frequent are felsic bands or lenses dominated by tabular alkali-feldspar segregated from the porphyritic granite that typically occur in the vicinity of microgranular enclaves (Fig. 2c); this association suggests segregation of solid material within the mush, probably caused by the introduction of hotter magma. Felsic segregations (mostly alkali-feldspar accumulations) are also associated with biotitic schlieren (Fig. 2e), and can be interpreted as products of aggregation of denser crystallized material in lower viscosity or higher temperature zones (Tobisch *et al.*, 1997; Collins *et al.*, 2006; Pons *et al.*, 2006). A distinctive feature is the occurrence of felsic segregations associated with elliptical biotite schlieren defining structures similar to disrupted pipe-vortex segregations (Fig. 2f; see Weinberg *et al.* 2001), which may be related to thermal plumes caused by heating of the granitic magma. In one locality, a steep ~40 cm wide banded schlieren occurs with alkali feldspar phenocrysts in a plagioclase–biotite-dominated matrix; its cumulate nature is emphasized by anomalously high REE, Zr, Ba, and Sr contents, reflecting the abundance of allanite and plagioclase.

Mica-rich enclaves

Biotite-rich enclaves are strongly foliated and display biotite alignment and granoblastic quartzo-feldspathic

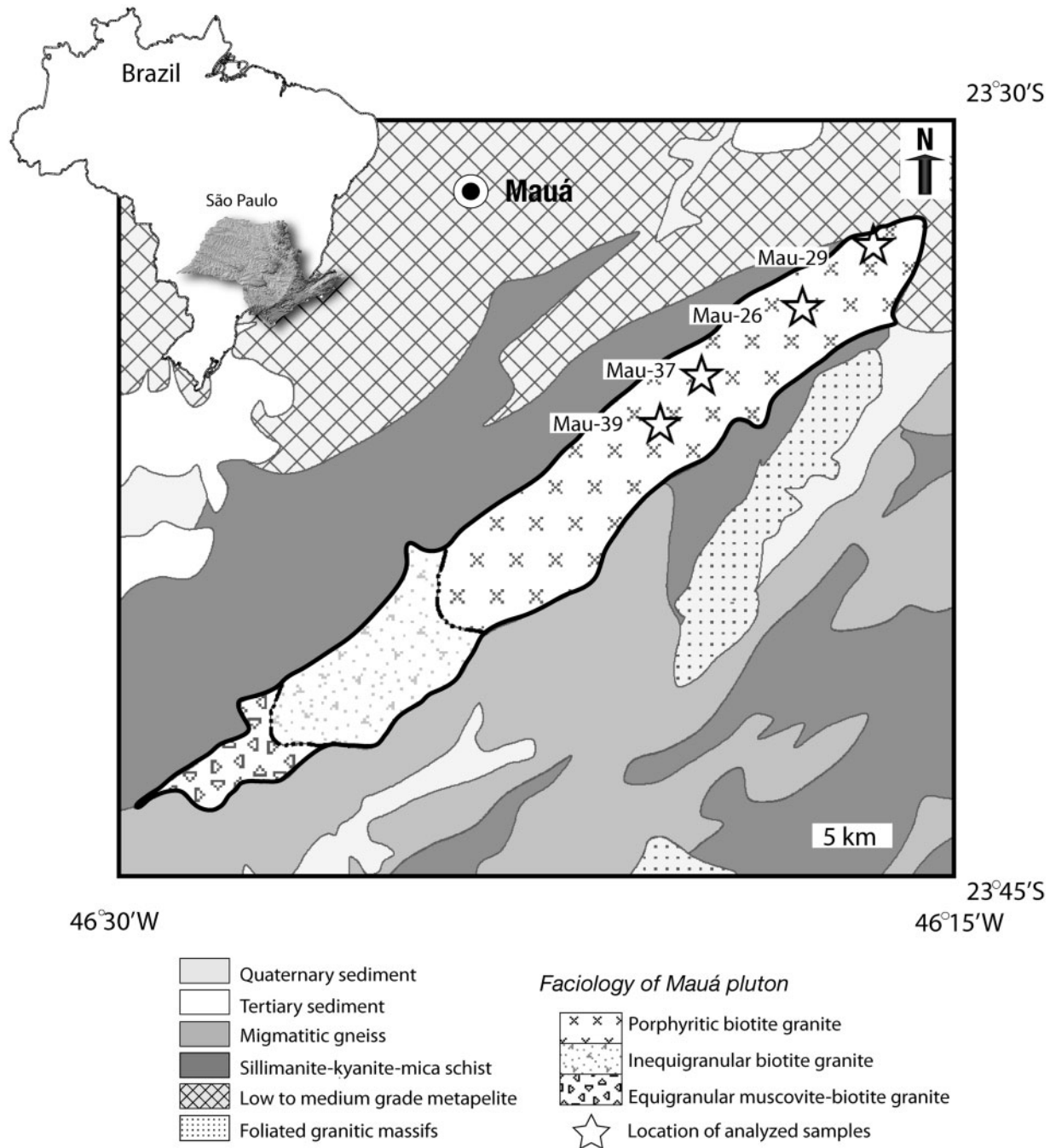


Fig. 1. Local geological map and sample location (modified from Theodorovicz *et al.*, 1992).

domains (Fig. 3a–f). Tabular, sheet-like shapes are often observed, with elongation parallel to the flow foliation in the porphyritic granite (Fig. 3a). Felsic mineral assemblages comprise (in order of decreasing abundance) quartz, alkali feldspar and plagioclase with a granolepidoblastic texture; biotite-rich domains surround granoblastic quartzo-feldspathic lenses. Late crystallized muscovite and abundant metamict allanite, apatite, and zircon

complete the mineral assemblage. A distinctive feature of these enclaves is that they are occasionally partly or totally included in small microgranitic enclaves (Fig. 3f).

Cumulate enclaves

An enclave with a coarser texture was found as an inner fragment within a typical microgranular enclave (Fig. 3h and i). It consists mainly of subidiomorphic biotite and

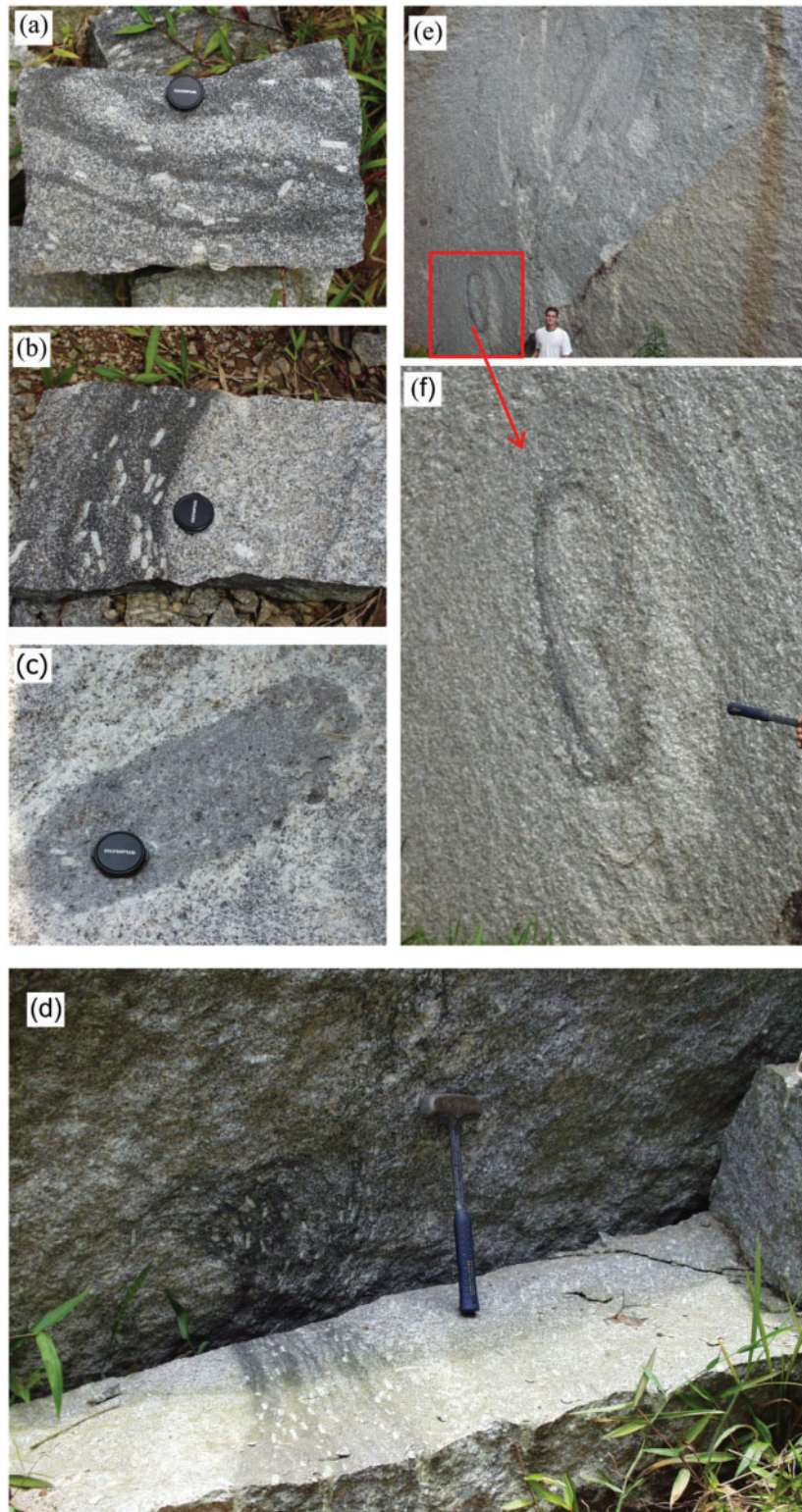


Fig. 2. Mineral segregations associated with porphyritic granite from the Mauá pluton. (a) Layered bands consisting of alternating biotite- and feldspar-rich layers; (b) cumulate band with phenocrysts parallel to the contact with porphyritic granite; (c) felsic microgranular enclave surrounded by feldspathic accumulation (note equigranular appearance of adjacent granite); (d) curved biotite–feldspar segregation with felsic concentration on concave side; (e, f) felsic segregations limited by schlieren and detail of ellipsoidal structure with internal and external parts limited by schlieren.

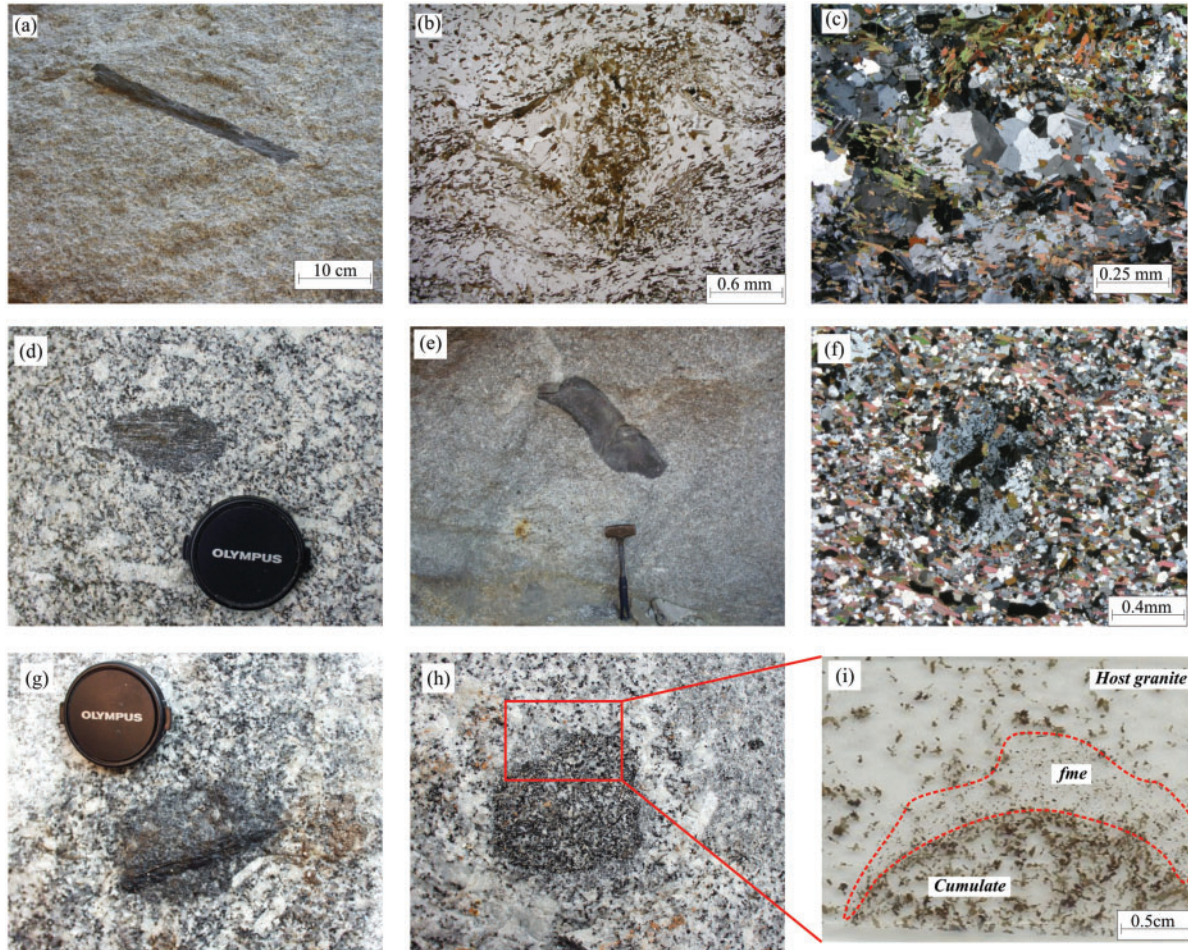


Fig. 3. Photomicrographs of enclave types in the Mauá pluton. (a) Mica-rich tabular enclave oriented along the flow foliation; (b, c) photomicrographs showing lepidogranoblastic texture, indicative of solid-state deformation; (d) lenticular enclave with gneissic texture; an abundant type in all outcrops; (e) massive mica-rich enclave with irregular shape associated with K-feldspar segregation limited by a biotite-rich granite; (f) detail of structure with poikiloblastic K-feldspar grain in fine-grained lepidoblastic matrix; (g) double enclave showing an inner mica-rich, sheet-like enclave enclosed by a microgranular ovoid enclave; (h) double enclave with coarser microgranitic enclave surrounded by a felsic microgranular enclave; (i) detail of the double enclave in (h). The area limited by the dashed line is a fine that surrounds an inner enclave of cumulate nature.

plagioclase, with xenomorphic quartz and rare alkali feldspar. In contrast to the mica-rich enclaves, this type has a preserved magmatic texture with no evidence of solid-state deformation and with normally zoned plagioclase crystals. At the contact with the outer enclave, there is a thin film of fine-grained material of similar composition to that of the other felsic microgranular enclaves. The classification as a cumulate enclave is based on petrographic and major element chemistry similarities to the cumulate bands.

Felsic microgranular enclaves

Felsic microgranular enclaves (fme) occur only in the porphyritic facies of the Mauá pluton. They have ellipsoidal shapes (aspect ratio varying from 2:1 to 3:1) with major axes ranging from 10 to 30 cm in length, and are frequently

aligned parallel to the flow foliation (Fig. 4). Some enclaves up to 1 m in length are observed. There are also some enclave swarms. The most evident difference between the fine and the host granites is their smaller grain size, which gives them a darker color (Fig. 4). Contacts are commonly sharp with rare cusped edges, which are better observed in thin section; chilled margins are rarely seen.

Modal estimates indicate rather homogeneous monzogranitic compositions with variations mainly related to the relative abundance of xenocrysts. In some cases, the xenocrysts are rare or very small (e.g. a few rounded mantled plagioclase crystals); such enclaves may be rich in biotite clots. As a means of distinction they are referred to here as equigranular enclaves. More abundant are 'porphyritic' enclaves, with abundant xenocrysts, dominantly of alkali feldspar. Variations in texture are related to

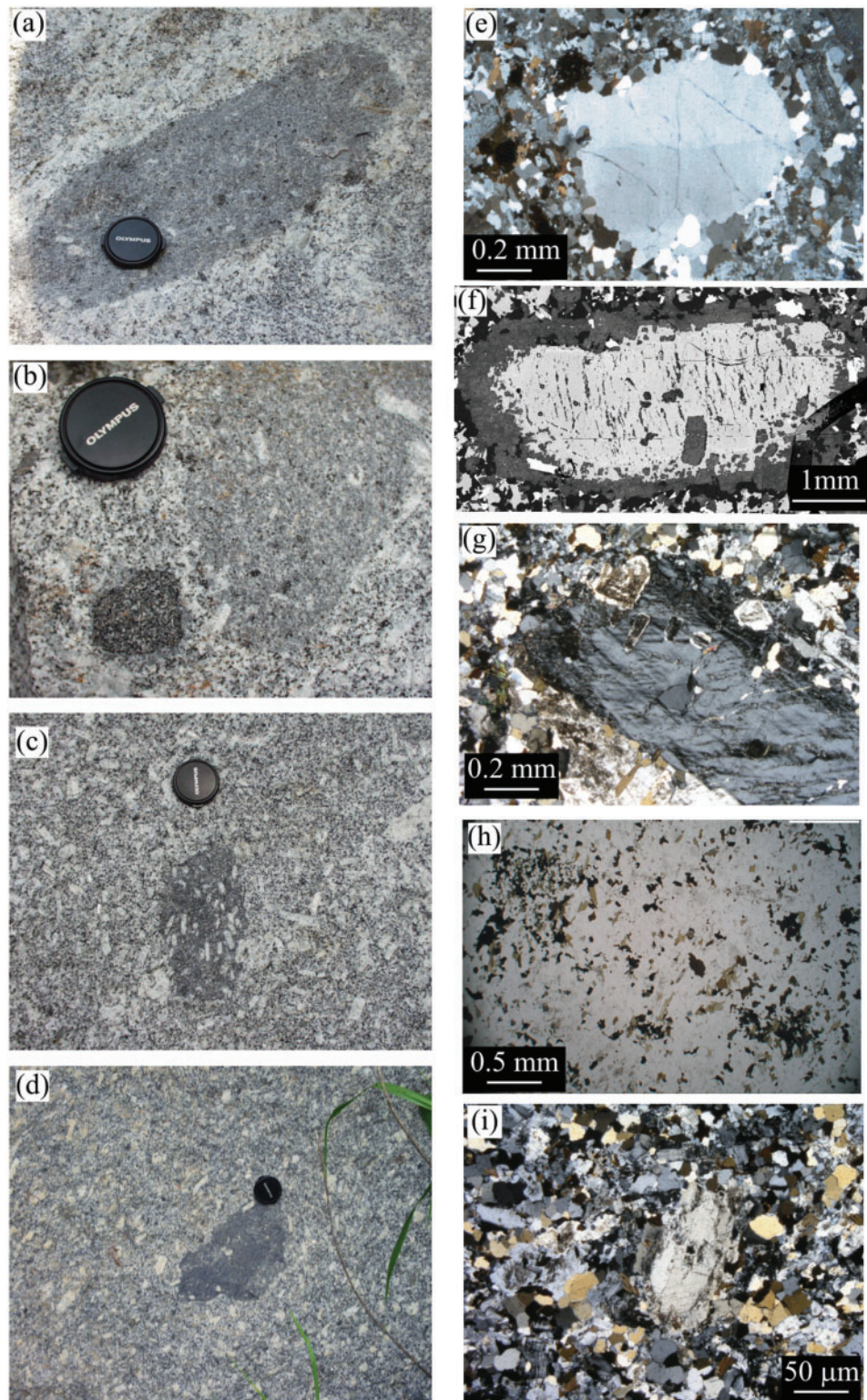


Fig. 4. Photomicrographs of felsic microgranitic enclaves and their textural relations. (a) An fine showing abundant biotitic clots and K feldspar xenocrysts of larger size closer to the enclave rim. (b) Double enclave with inner enclave being disrupted from larger fine outer enclave; disruption is probably caused by rheological divergences, suggesting solid state for inner enclave. (c) An fine with high concentration of xenocrysts with orientation parallel to the host-granite foliation; (d) zoned fine in which the darker central part contains rare xenocrysts whereas the outer part is progressively paler and richer in xenocrysts; irregular boundaries suggest interaction in a plastic state; (e) xenocrystic quartz with undulose extinction; (f) rapakivi texture in alkali feldspar xenocryst; (g) overgrowth on feldspar xenocryst with poikilitic texture; (h) biotite-rich clots formed by xenomorphic biotite, apatite and feldspar; (i) plagioclase xenocryst with alteration ring marking the beginning of poikilitic overgrowth.

Table 1: Textural relationships of main mineral phases in the fme

Mineral, size	Mode of occurrence	Inclusions	Disequilibrium textures
<i>Quartz</i>			
Few μm -2 mm	Matrix: Interstitial, xenomorphic, no solid-state deformation, occasionally poikilitic Xenocryst: rare, rounded, with evident solid-state deformation (e.g. undulose extinction and subgrain formation; Fig. 4e)	Absent	Xenocrysts may show rims marked by concentration of small circular plagioclase crystals
<i>Biotite</i>			
20-50 μm	Main mafic mineral, elongated idiomorphic crystals with strong pleochroism widespread	Zircon, abundant needle apatite and Fe-Ti oxides	May occur as circular clots (Fig. 4h) where it appears as intergrowths with apatite
<i>Alkali feldspar</i>			
Few μm -2 cm	Xenocrysts: crystals with size contrasted to matrix and xeno-morphic overgrowths, of 0.5-1.5 cm, with inclusion-free cores Matrix: Xenomorphic crystals with poikilitic rims	Overgrowths with abundant inclusions of quartz, plagioclase and earlier alkali feldspar, may result in mosaic-like textures Absent	Rapakivi texture is rare and was observed only in equigranular enclaves (Fig. 4f)
<i>Apatite</i>			
10-30 μm	Needle-like habit, usually included in feldspars and biotite	Absent	

differences in the shapes and distribution of the xenocrysts; these occur either as randomly distributed tabular crystals or oriented parallel to the flow foliation of the host granite and the host enclave major axis. The xenocrysts do not seem to have any particular pattern of distribution within the enclaves; for example, commonly the xenocrysts are not more abundant at the borders of the enclave as observed in some other occurrences of microgranular enclaves (Browne *et al.*, 2006).

The petrographic descriptions presented here focus on mineral textures within the microgranitic enclaves. Despite differences in rock texture, the constituent minerals show similar textural relationships. An integrated petrographic description is presented in Table 1; representative textures are illustrated in Fig. 4. Because the present study focuses on plagioclase textures and corresponding chemical signatures, the textural relationships of this mineral are described in more detail below.

ANALYTICAL METHODS

Whole-rock geochemistry and Sr isotopic data

Whole-rock samples were analyzed by X-ray fluorescence (XRF) at the Instituto de Geociências, Universidade de São Paulo (IGc-USP), Brazil. Detailed petrographic

examination of thin sections and bulk-rock major element compositions were used as criteria to select samples for inductively coupled plasma mass spectrometry (ICP-MS) trace element analysis using a Plasma Quadrupole MS ELAN 6000 (Perkin Elmer). Samples were prepared following acid digestion in Parr-type bombs using concentrated nitric and hydrofluoric acids. Digestion was conducted at high temperature (around 200°C) in a microwave oven over 5 days to guarantee dissolution of resilient minerals such as zircon. The effectiveness of this approach was verified by comparing the Zr abundances obtained by ICP-MS with those determined by XRF; these are not significantly different.

Whole-rock Sr isotope analyses of selected samples were performed at the Centro de Pesquisas Geocronológicas (CPGeo), IGc-USP, Brazil, by TIMS. Sample preparation followed the same steps as used in the ICP-MS procedures, differing only with respect to digestion duration and temperature (10 days at 160°C). Chemical separation of Sr was carried out using conventional cation columns containing AG 50 WX8 and LN resins; samples were previously mixed with a $^{84}\text{Rb}/^{87}\text{Sr}$ spike. Isotopic data were obtained using a Multi Collector Mass VG 354 Spectrometer; Rb/Sr ratios from the XRF data were used for isotope ratio age corrections.

Laser ablation ICP-MS

Laser ablation analyses were conducted on thin sections ~120 µm thick, polished to a 1 µm finish and cleaned in an ultrasonic bath filled with milliQ water. *In situ* trace element abundances in plagioclase were determined at the Radiogenic Isotope Facility (RIF), Department of Earth and Atmospheric Sciences, University of Alberta, Edmonton, Canada, using a Perkin Elmer Elan6000 Quadrupole ICP-MS system, coupled to a frequency quintupled ($\lambda = 213$ nm) Nd:YAG laser ablation system. Eight plagioclase crystals were analysed from enclaves that show the most variable major element compositions. Concentrations were calculated using the NIST SRM 612 international standard glass for external calibration, and Ca as the internal standard determined by electron microprobe analysis for the unknowns. Data reduction was conducted using the Glitter[®] laser ablation software (Macquarie University).

Laser ablation-multi-collector ICP-MS

The same thin sections as used for *in situ* trace element analyses were employed for Sr isotope determinations at the RIF. In general, spots for laser ablation analysis were restricted to areas of plagioclase crystals characterized by low Rb/Sr values (<0.05) to minimize the isobaric correction of ⁸⁷Rb on ⁸⁷Sr. Ablations were carried out using a 160 µm beam diameter with variable ablation times (30–60 s; mainly dependent on Sr ion signal intensity). Ramos *et al.* (2004) argued for a minimum of ~1 V ion signal to obtain high-precision isotopic measurements. The Sr ion signal intensities for the analyses conducted here varied from 0.7 to 1.3 V, and these produced Sr isotope measurements with associated 2σ uncertainties well below the total isotopic variation recorded between cores and rims of single plagioclase crystals. The corrections included: the isobaric interference of ⁸⁷Rb on ⁸⁷Sr by the simultaneous acquisition of the ⁸⁵Rb ion signal; ⁸⁴Kr, ⁸⁶Kr and ArO₃ interferences eliminated with a 30 s on-peak baseline measurement prior to laser ablation, and monitoring of doubly charged REE ion signals at half-mass positions (Paton *et al.*, 2007). A modern-day coral (Indian Ocean) was used as an external standard (Bizzarro *et al.*, 2003; Schmidberger *et al.*, 2003). Details of the analytical protocol have been given by Schmidberger *et al.* (2003). Analytical conditions are summarized in Table 2.

WHOLE-ROCK GEOCHEMISTRY AND Sr ISOTOPE COMPOSITIONS

Previous geochemical studies by Filipov & Janasi (2001) proposed that the Mauá granites evolved by fractional crystallization involving extraction of plagioclase and biotite plus accessory Fe–Ti oxides, apatite, zircon and, in the

Table 2: Operating conditions and analytical parameters for laser ablation analysis

Multi-collector mass spectrometer	
Model	MC ICP MS Nu Plasma from NU Instruments Ltd.
Gas flows	Coolant (plasma) Ar 13 l/min Auxiliary Ar 1.0 l/min
Forward power	1300 W
Sample transport	He 1.0 l/min, Ar 3.2 l/min (DSN-100)
Laser ablation system	
Model	New Wave Research UP213 with aperture imaging
Wavelength	213 nm
Pulse width	3 ns
Pulse energy	0.5 (0.002 mJ/pulse)
Energy distribution	Homogenized, flat beam, aperture imaged
Energy density	11 J/cm ²
Focus	Fixed at surface
Repetition rate	5 Hz for standard, 10 Hz for plagioclase
Crater diameter	160 µm for Sr isotopes, 120 µm for trace elements

late stages, a LREE-bearing phase (allanite and/or monazite). Open-system processes involving contamination with the surrounding country rocks were suggested based on the geochemical trends in the border facies rock units but not modeled because of a lack of isotope data.

The fine and host porphyritic granites (HG) are remarkably similar in composition. They are marginally peraluminous with $1 < A/CNK < 1.05$, low mg-number ~0.20–0.23 and SiO₂ contents ranging from 68 to 71 wt % (Table 3, Fig. 5). On average, the enclaves are slightly more mafic, as shown by a tendency to have lower silica and higher Mg-number, Fe, Mg, Ti and P contents; however, they also have higher K₂O contents. The host porphyritic granites have systematically higher Ba and Sr contents, which might be a reflection of feldspar accumulation not observed for the fine. The more felsic granites from the SW portion of the pluton have highly differentiated compositions with 76 wt % SiO₂, 40 ppm Ba, 20 ppm Sr and mg-number as low as 0.10. The REE patterns of both the porphyritic granites and the fine are moderately fractionated with (La/Yb)_N = 8–16 and 12–18, respectively; the leucogranites show typical seagull-wing patterns indicative of LREE fractionation (Filipov & Janasi, 2001).

Biotite-rich, sheet-like enclaves are highly potassic (7.6–8.5 wt % K₂O) and have mg-number much higher than that of the fine (>35). The inner enclave from double-enclave sample Mau-39B may be interpreted as a disrupted cumulate (autolith), as shown by a comparison of its major-element composition with that of a cumulate

Table 3: Representative chemical analyses for host granites and various enclave types from Mauá pluton

Sample:	Porphyritic biotite granites					Equigranular granites			Felsic magmatic enclaves					Cumulate	Mica-rich enclaves		
	1A	4	11A	28	29	6B	8A	5	2A	3B	26	37B	39B	22b	37A	39A	10B
SiO ₂	71.68	70.54	71.04	70.78	70.59	75.40	73.61	74.33	69.85	70.05	68.75	70.55	69.58	59.31	54.89	59.53	56.72
TiO ₂	0.34	0.45	0.42	0.403	0.39	0.12	0.25	0.05	0.45	0.43	0.495	0.436	0.495	1.33	0.866	1.764	0.90
Al ₂ O ₃	14.07	14.01	14.15	13.73	14.02	12.24	13.08	13.61	14.54	14.28	14.51	14.03	14.13	15.05	18.86	14.41	17.05
Fe ₂ O ₃	3.27	3.90	3.65	3.64	3.59	1.71	2.70	1.34	3.80	4.01	4.09	3.66	4.01	11.18	8.68	11.36	9.64
MnO	0.06	0.07	0.07	0.060	0.07	0.06	0.06	0.14	0.07	0.06	0.065	0.062	0.065	0.18	0.139	0.202	0.16
MgO	0.42	0.50	0.48	0.45	0.42	0.09	0.27	0.03	0.56	0.60	0.55	0.50	0.55	1.52	2.05	1.66	2.27
CaO	1.58	1.72	1.70	1.72	1.75	0.67	1.22	0.10	1.64	1.78	1.47	1.61	1.64	2.54	1.89	3.15	0.94
Na ₂ O	3.40	3.16	3.25	3.33	3.23	3.36	3.14	4.10	3.29	3.21	2.97	3.03	3.02	2.97	3.39	2.60	2.24
K ₂ O	4.99	4.80	5.03	4.58	5.13	4.67	4.88	4.50	5.22	4.98	5.86	4.93	5.18	5.03	7.60	3.41	8.51
P ₂ O ₅	0.17	0.18	0.17	0.163	0.16	0.03	0.10	0.02	0.16	0.19	0.191	0.141	0.175	0.54	0.109	0.689	0.09
LOI	0.65	0.62	1.44	0.50	0.86	1.16	0.92	1.25	0.38	0.39	0.480	0.360	0.42	0.32	0.720	0.600	
Total	100.64	99.94	101.41	99.36	100.21	99.50	100.24	99.48	99.96	99.98	99.43	99.31	99.27	99.97	99.19	99.38	98.52
Rb	226	213	209	205	197				205	231	181	257	241	338	230	354	543
Ba	717	1090	888	1068	1101	153	426	63	604	636	690	690	548	802	292	568	708
Sr	162	186	167	178	184	45	104	17	149	150	117	137	136	143	113	158	128
Zr	230	266	237	232	239	74	167	54	246	236	349	234	294	870	152	118	140
La	60.7	65.3	56.00	73.60	55.15	23	51	22	52	64	63.6	59.8	64.5	243	30.5	74.6	31.00
Ce	106.8	136.14	114.89	134.00	97.8				127.2	122.8	163	132	146	507	94.6	173	64.0
Pr	12.37	15.28	12.76	16.30	12.96				14.38	13.70	16.1	13.7	15.2	54.3	9.62	20.0	
Nd	41	52.59	46.51	57.20	45.4	33.0	52.0	17.0	47.7	44.2	62.5	51.0	57.1	207	38.8	84.7	26.0
Sm	7.9	9.15	8.75	10.40	8.35	5.69	8.79	4.86	8.90	8.30	11.5	8.85	10.18	33.6	8.11	17.7	4.83
Eu	1.33	1.41	1.18	1.56	1.37	0.50	1.20	0.40	1.24	1.21	1.26	1.11	1.15	1.55	1.57	1.56	1.20
Gd	6.30	7.53	6.41	8.54	7.19				7.30	6.40	8.72	6.73	7.96	23.5	6.44	15.0	
Tb	1.00	1.05	1.15	1.23	1.05	1.90	1.50	1.70	1.10	1.00	1.26	0.94	1.12	3.15	0.94	2.17	1.70
Dy	4.90	5.35	6.09	6.61	5.82				5.50	4.70	6.65	4.95	5.94	15.71	5.14	11.48	
Ho	1.00	1.11	1.21	1.33	1.31				1.20	1.10	1.29	0.97	1.16	2.95	1.06	2.26	
Er	3.10	3.05	3.23	3.53	3.98				3.40	3.30	3.42	2.57	3.07	8.09	2.94	5.77	
Yb	2.90	2.65	0.39	3.26	4.29	3.70	4.20	6.70	2.90	2.70	2.73	2.15	2.58	6.22	2.79	4.29	5.30
Lu	0.42	0.39		0.50	0.73	0.49	0.56	0.92	0.43	0.41	0.39	0.31	0.37	0.91	0.42	0.58	0.87
⁸⁷ Rb/ ⁸⁶ Sr				3.20			52.77	4.60		5.39		5.29		8.68		11.96	
⁸⁶ Sr/ ⁸⁷ Sr meas.				0.7379			1.1783	0.7489		0.7567		0.7563		0.7883		0.8077	
⁸⁶ Sr/ ⁸⁷ Sr ₅₉₀				0.7110			0.7343	0.7102		0.7106		0.7110		0.7140		0.7077	

Sample names lacking prefix Mau; sample names in italics correspond to data from Filipov & Janasi (2001).

sample (Mau-22b, Table 3); differences in trace element abundances such as lower LREE, Zr and Th, indicate mineral accumulation before zircon and allanite saturation.

Representative Sr isotope analyses of typical rock types from the Mauá pluton are presented in Table 3. Initial ratios were calculated for the magmatic age of 590 Ma (⁸⁷Sr/⁸⁶Sr_i, Table 3); as with the major and trace element geochemistry, the porphyritic granites and fine have similar compositions; ⁸⁷Sr/⁸⁶Sr_i varies from 0.7102 to 0.7110 for the enclaves compared with 0.7110 for the porphyritic granite. Sample Mau-5a, an extremely fractionated

leucogranite, has a calculated initial ⁸⁷Sr/⁸⁶Sr = 0.7346, which is imprecise given the high Rb/Sr ratio of this sample (17.6).

PLAGIOCLASE CHEMICAL AND ISOTOPIC ZONING

Description of the selected samples

Plagioclase crystals from four samples were selected for detailed trace element and Sr isotopic analyses. They were

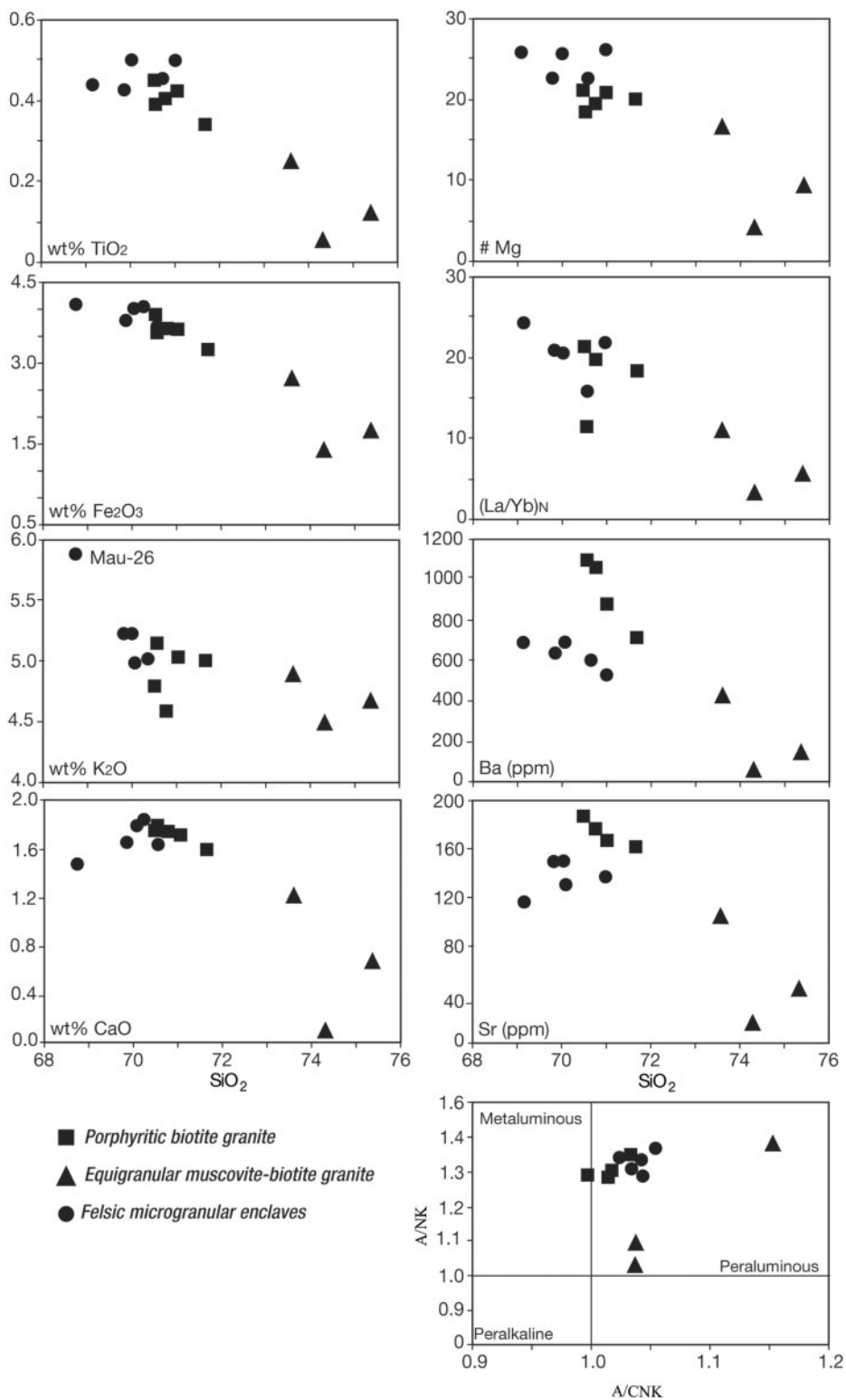


Fig. 5. Major and trace element variation diagrams and ASI classification for fine and host granites.

chosen using as criteria the presence of xenocrysts, resorption zones and/or multiple zoning patterns in a single crystal, and the range of An variation (greater than 5%). The crystals show very complex compositional zoning patterns with An-rich cores followed by diffusely zoned resorption zones and normally zoned rims. There are important differences in zoning style between samples as summarized in Table 4. In addition to those from enclaves, a plagioclase grain from a typical porphyritic granite (Mau-29) was studied for comparison. The analysed crystal is 2 mm wide, equidimensional and homogeneous, exhibiting minor normal zoning (An 27–25). Overgrowths (An 22–23) surround a zone rich in tiny inclusions and are poikilitic.

Compositional zoning

All the analyzed plagioclase crystals have similar major element compositions and zoning patterns; the only significant differences are the variations in An content, as described above. MgO, K₂O and Fe₂O₃ abundances are almost constant (see Supplementary Data, available for downloading at <http://www.petrology.oxfordjournals.org>). An increase in Or content is observed in the overgrowths, accompanied by a decrease in Fe₂O₃ and MgO and an increase in TiO₂. In contrast, LA-Quadrupole-ICPMS analyses reveal wide variations in trace element contents in all crystals, regardless of the zoning pattern or enclave type. Figure 6 illustrates trace elements profiles for crystals from sample Mau-26 and crystal Mau-37C1; with the data reported in Table 5 (except for those elements whose contents were close to the detection limit). The complete trace element dataset, including data for Mau-29 and Mau-39B, errors and detection limits is provided as Supplementary Data.

Crystals from Mau-26 show very similar trace element profiles, with patterns in cores–outer cores distinct from those observed in the rims. Ba, Σ LREE (total LREE) and Sr contents increase towards the outer cores whereas Pb and the Sr/Ba ratio decrease. The resorption zones are characterized by intermediate values between those observed for the cores and rims, the latter exhibiting a progressive decrease in Ba, Σ LREE, and Sr and an increase in Pb. Most trace elements define ‘M-shape’ profiles with mirrored behavior observed for Pb. (La/Sm)_N [where subscript N indicates normalization to the chondritic values of McDonough & Sun (1995)] shows the same profile (not illustrated), with lower values within the inner cores (~20 for both crystals) whereas the outer cores and rims show homogeneous high values (~30).

Despite the profile similarities exhibited by Ba and Sr, the ratio Sr/Ba mimics the Pb profile. Impoverishment towards the rims is more pronounced for Ba than for Sr, whereas enrichment towards the outer cores is more prominent for the former. In both crystals, the trace element contents in the rims are closest to the values obtained for

the matrix crystals, except for Σ LREE in Mau26-C2, where values are higher than those of the matrix.

Enclave Mau37 contains relatively small, equidimensional plagioclase grains and the profile obtained for crystal Mau-37C1 shows much less regularity than those in Mau-26. Trends are observed solely for La, Ce and Σ LREE, Ba and Sr, as there is a core-resorption zone decrease. Pb also exhibits a mirrored profile, but in a more subtle way than observed for Mau-26.

There are important dissimilarities between profiles, especially evident for (La/Sm)_N ratios and Sr. Mau37-C1 shows an increase in (La/Sm)_N (not shown) and a homogeneous Sr content, whereas Mau37-C2 shows the opposite trend for (La/Sm)_N and an increase in Sr towards the rim. The crystals also show significant variations in absolute contents for all trace elements except Sr, with Mau37-C1 showing higher values. Ba/Sr is lower in the cores, as observed for Mau-26.

A crystal from the outer enclave of Mau-39B (not shown) has similar trace element patterns that resemble those of the samples described above, with a core rich in La, Ce, Σ LREE, Ba and Sr that decrease progressively towards the rim. The (La/Sm)_N ratio is notably homogeneous and the crystal has extremely low Ba and Sr contents compared with other samples, although with similar profiles.

Isotope zoning

Variations in ⁸⁷Sr/⁸⁶Sr_i in plagioclase crystals are relatively large (0.7104–0.7154; Table 6) and well outside the associated (2 σ) uncertainties. Rim-to-rim profiles are shown in Fig. 7 for all the analysed crystals, with the exception of crystals C2 and C3 from Mau39B, for which back-scattered electron (BSE) images labelled with associated Sr isotope ratios are illustrated instead, in view of the irregularity in isotopic signature. Table 6 presents all the data, including the ⁸⁷Rb/⁸⁶Sr ratios used in the calculation of ⁸⁷Sr/⁸⁶Sr_i.

For samples Mau-37 and Mau-26 the An-rich cores are more radiogenic compared with the rims, even though they exhibit different absolute values (⁸⁷Sr/⁸⁶Sr_i = 0.7115–0.7127 in Mau-26; 0.7125–0.7154 in Mau-37). The isotopic variation is positively correlated with the decrease in An content towards the rims, which are significantly less radiogenic, once again with differences in their absolute values (0.7095 < ⁸⁷Sr/⁸⁶Sr_i < 0.7118; higher values for Mau-26).

The outer cores, present only in Mau26-C1 and C2, show an increase in ⁸⁷Sr/⁸⁶Sr_i relative to the values observed for the cores. This increase is followed by the typical rimward decrease, defining an ‘M-shape’ profile (more subtle for Mau26-C2). The only exception is Mau26-C3 from the same sample, which appears to have an irregular core not surrounded by an outer core.

Table 4: Main textural features of analyzed plagioclase crystals

Sample:	Mau-26		Mau-37		Mau-39B		
Crystal:	Mau-26C1	Mau-26C2	Mau-37C1	Mau-37C2	Mau-39BC1 (outer enclave)	Mau-39BC2 (inner enclave)	Mau-39BC2 (contact zone)
Core	Tabular with rounded vertices, inclusion-free (An 30–35)	Diffuse zoning pattern does not individualize crystal regions	Inclusion-rich, boxy-cellular texture (An 35–42) with tabular contours	Corroded with higher An (32), texture irregular but not boxy or patchy	Rounded, inclusion-free; An 28–32	Inclusion-rich, boxy-cellular texture; (An 37–42), irregular, rounded terminations	Wide, An-rich (26–28), with irregular contours; inclusion-rich, but not patchy
Outer core	Normally zoned, pattern increasingly parallel to core terminations (An 26–30)		Absent	Absent	Absent	Absent	Absent
Resorption zone	Diffusely zoned with An contents in same range as in outer cores or slightly lower		Diffusely zoned with lower An content cores (An ~27–30); corrodes boxy cores forming irregular contacts	Diffusely zoned with terminations parallel to core with corrosive inner contacts (An ~27)	Diffusely zoned after core, with no change in An content	Irregular, discontinuous and has An values identical to thin rims (An 25–26)	Absent
Rim	Zonation increasingly parallel to external crystal shape (An25–27)		Normal zoning parallel to crystal shape (An 25–30)	Similar to Mau-37C1	Very homogeneous; width >800 µm, An 24–26	Homogeneous zoning and irregular limits; very thin (~40 µm)	With lower An content (24–26) comprising <15% of the grain area
Overgrowth or external RZ	Xenomorphic up to 20 µm wide with An <20; crosscut rims and is marked by presence of several small inclusions		Limited extension (~23 µm) and inclusion-free	Similar to Mau-37C1; An ~20	An-poor, irregular and poikilitic with variable amount of inclusions (less frequent and sparser than in Mau-26)	Absent	Xenomorphic, An-poorer (<22%)
Sample description	Porphyritic enclave with abundant alkali feldspar megacrysts (1–2 cm in greater dimension) and subidiomorphic plagioclase larger (0.8–3 mm) than matrix (0.3 mm)		Inequigranular enclave with rare alkali feldspar megacrysts (usually <0.5 cm, with plagioclase overgrowths and ocellar or rapakivi texture) and smaller		Double enclave with an inner enclave of coarser, equigranular texture and similar to cumulate bands, and the host enclave macroscopically similar to the porphyritic enclaves plagioclase grains with predominant equidimensional shapes		

The rimward decrease culminates in the lowest ratio for sample Mau-26 (0.7104 and 0.7107).

Plagioclase crystals from Mau-37 display analogous zoning patterns with cores showing high $^{87}\text{Sr}/^{86}\text{Sr}_i$ values followed by a continuous decrease towards the rim, both core and rim recording a similar range of values to those observed for enclave Mau-26. It should be pointed out,

however, that the $^{87}\text{Sr}/^{86}\text{Sr}_i$ core value for crystal Mau37-C1 is associated with higher uncertainty, because of a higher Rb/Sr ratio, which results in a greater correction of the ^{87}Rb isobaric ion signal overlapping that of ^{87}Sr . The isotopic signature of crystal Mau37-C2, which shows a similar zoning pattern and has no alteration, may be a better estimate of the characteristic isotopic signature of the

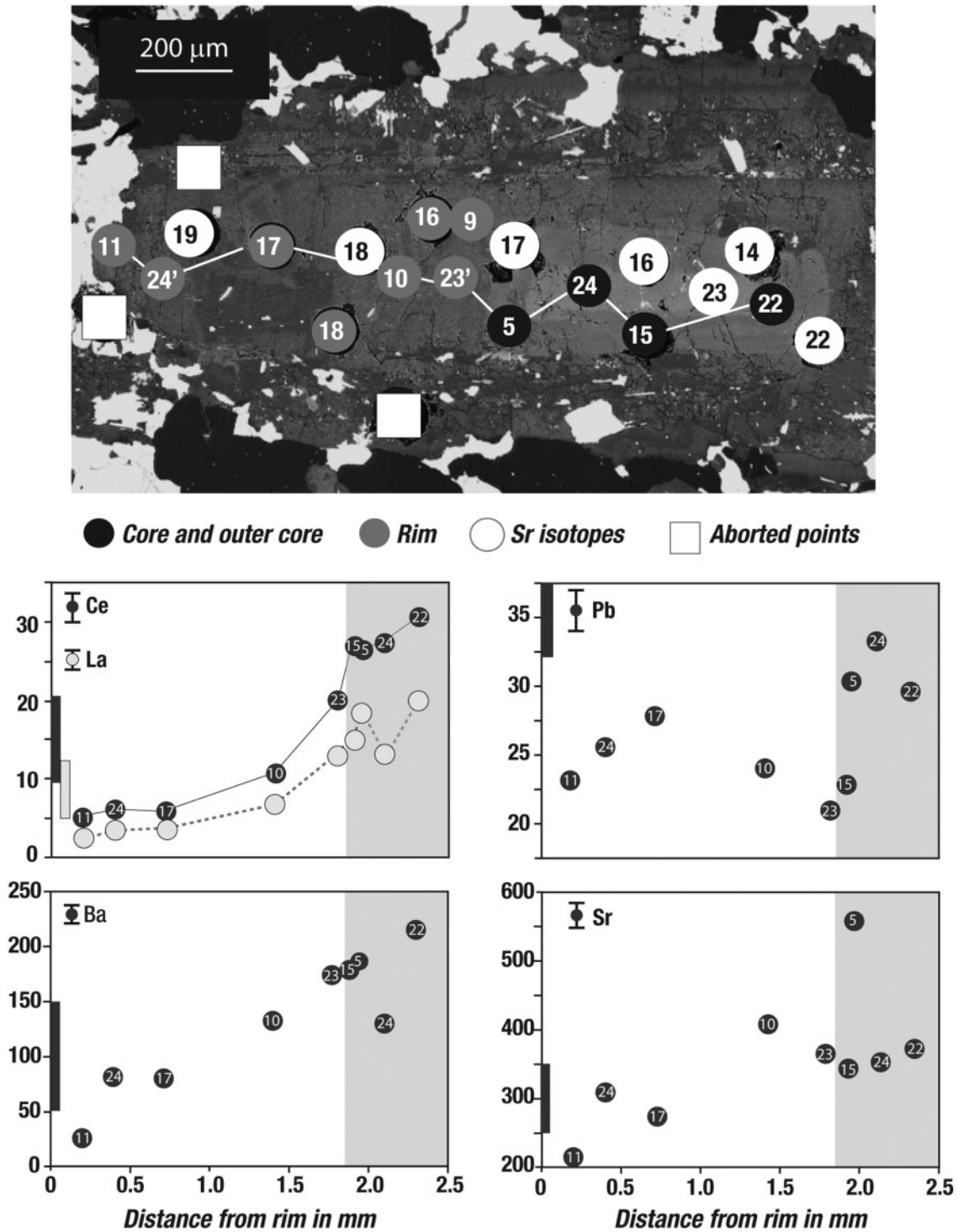


Fig. 6. Trace elements profiles for plagioclase xenocrysts from samples Mau26 (a, b) and Mau-37 (c); element concentrations in ppm and distance in mm. Shaded area represents the core and outer core regions; grey vertical bands close to the axis are the range in values registered by the matrix crystals. Numbers indicate analysis points.

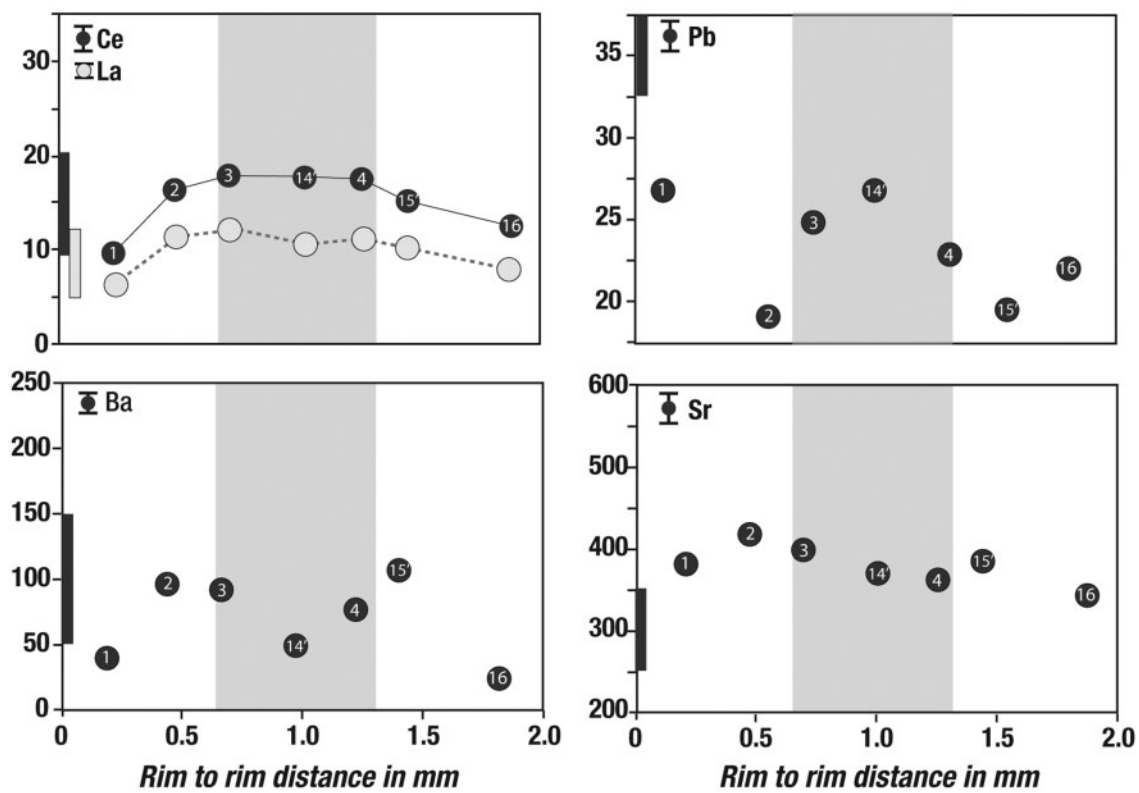
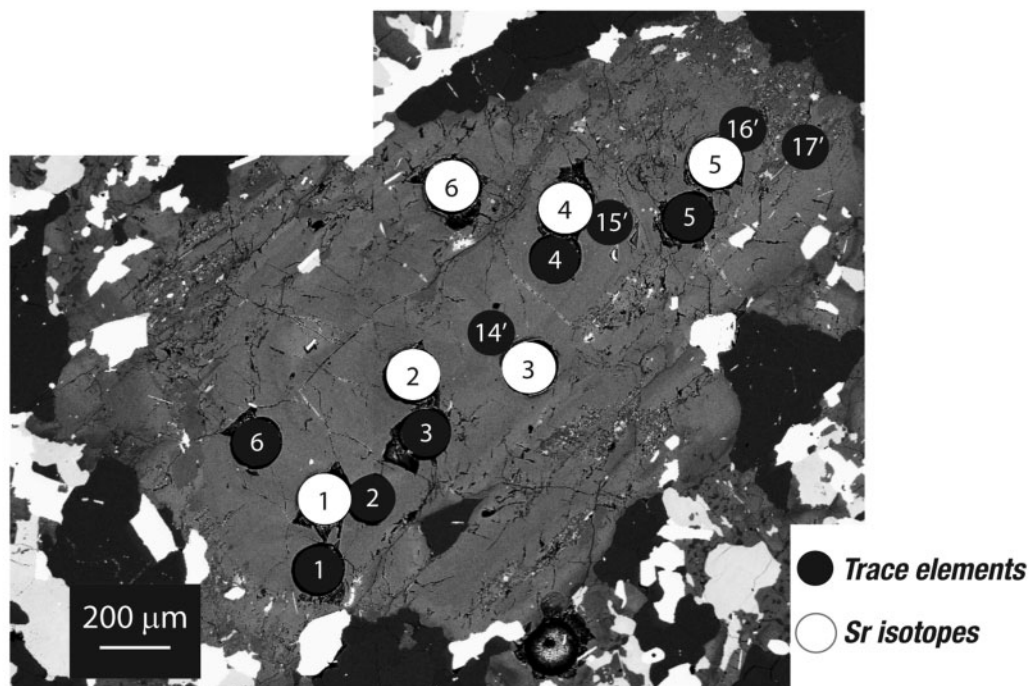


Fig. 6. Continued.

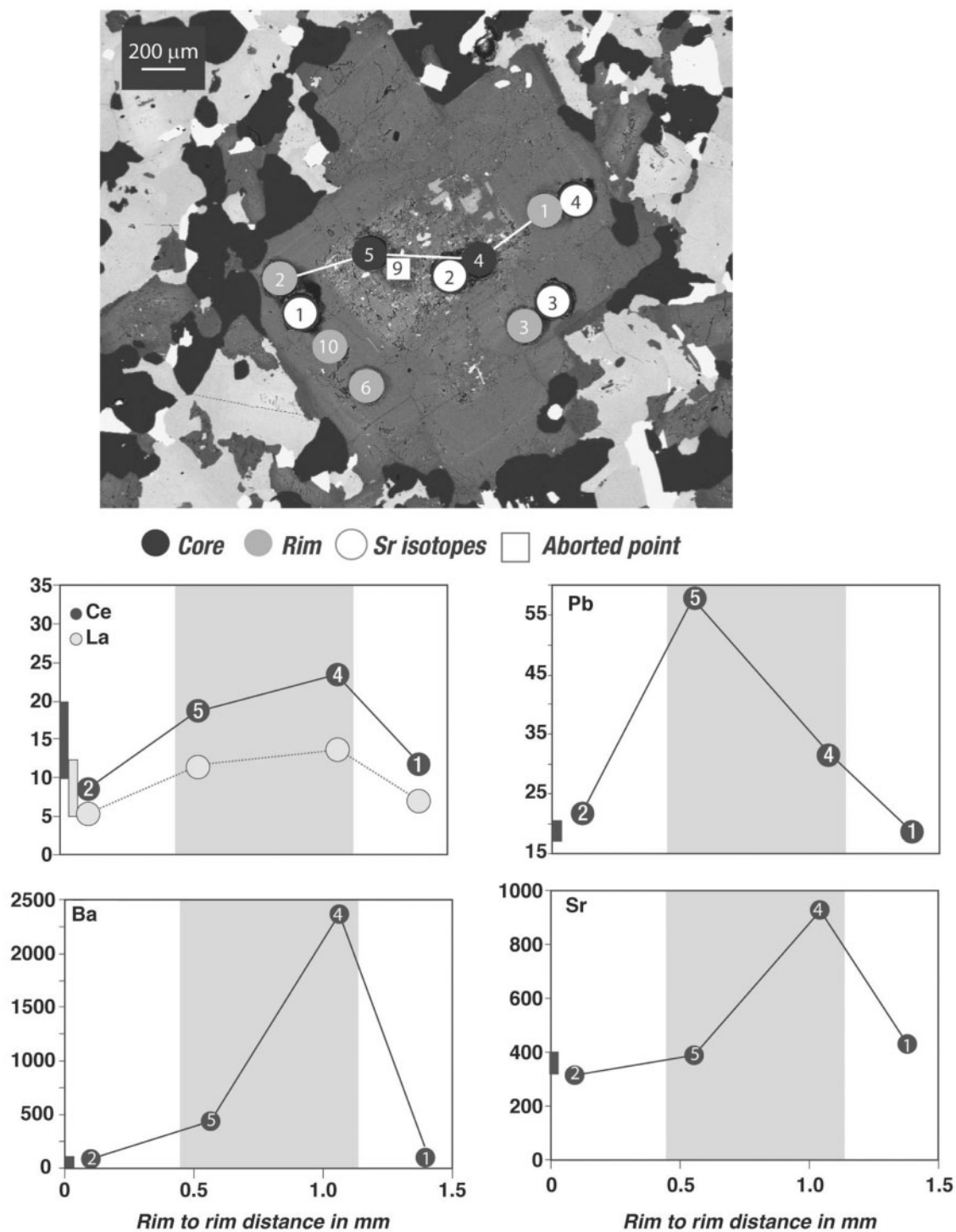


Fig. 6. Continued.

cores in Mau37; its $^{87}\text{Sr}/^{86}\text{Sr}_i$ of 0.7125 is similar to that observed for sample Mau-26.

The crystals from Mau-39B (the double enclave) exhibit a completely different isotopic profile. The plagioclase

crystal from the inner enclave shows a very complex pattern of $^{87}\text{Sr}/^{86}\text{Sr}_i$ variation with the core region having less calcic patches with high Sr isotopic ratios (0.7129) whereas more An-rich patches have lower $^{87}\text{Sr}/^{86}\text{Sr}_i$ between

Table 5: Representative trace element analyses for crystals from samples Mau-26 and Mau-37

Spot	Mg	Ti	Rb	Sr	Y	Zr	Nb	Ba	La	Ce	Pr	Nd	Sm	Eu	Gd	Pb	Th	U
<i>Mau-26 Crystal 1</i>																		
11	39.02	13.61	2.82	214.10	0.60	1.38	0.02	26.1	2.63	5.29	0.48	1.70	0.33	0.80	0.36	24.29	0.03	0.12
24*	2.53	20.35	0.13	308.84	0.12	0.19	<0.07	82.0	3.61	6.23	0.49	1.73	<0.42	2.25	0.14	26.05	0.43	0.02
17	23.39	17.76	4.47	273.98	0.14	0.19	0.03	78.5	3.62	5.85	0.48	1.47	0.27	1.46	0.13	27.78	0.56	0.03
10	26.51	25.13	1.02	406.04	0.24	0.57	0.01	130.6	6.87	10.49	0.89	2.64	0.27	2.25	0.26	25.00	0.03	0.03
23	2.79	18.49	0.63	365.61	0.19	0.21	<0.03	173.7	13.00	20.00	1.07	3.28	<0.51	2.55	0.31	22.53	1.30	<0.01
15	32.51	45.49	0.44	344.50	0.77	1.69	0.03	179.6	15.00	26.76	1.72	6.27	1.06	1.99	0.49	24.00	1.67	0.22
05	41.26	55.58	2.00	556.97	0.42	0.18	0.01	185.0	18.61	26.65	2.11	6.60	0.79	3.91	0.37	29.74	0.04	0.06
24	65.78	64.00	1.20	350.92	2.12	0.80	2.30	128.2	13.32	27.39	1.88	5.23	0.72	1.84	0.33	31.80	0.03	0.23
22	12.58	54.63	0.50	374.67	0.24	0.30	0.06	213.5	20.00	30.72	2.21	5.99	1.00	2.72	0.53	29.10	0.29	<0.01
<i>Mau-26 Crystal 2</i>																		
1	4.75	83.00	<0.25	330.31	0.23	0.08	<0.01	80.1	6.36	9.44	0.71	2.19	0.27	1.84	2.10	23.23	0.44	<0.00
2	18.14	82.04	0.20	373.49	0.44	0.15	<0.02	125.3	11.23	16.40	1.25	3.62	0.45	2.10	1.94	21.57	0.93	0.01
3	11.83	54.20	0.15	350.05	0.45	0.82	0.03	118.0	11.90	17.15	1.36	10.02	0.70	2.15	1.47	23.90	6.05	0.08
4	10.32	43.26	0.97	307.07	0.41	0.05	<0.02	106.9	11.02	17.25	1.34	3.65	0.48	2.24	0.81	24.61	0.22	0.02
14*	2.22	12.58	0.16	314.71	2.19	0.59	<0.08	85.5	10.66	17.41	1.58	5.91	1.28	2.16	0.75	26.50	0.53	<0.02
15*	11.26	14.60	0.91	335.25	0.23	<0.08	<0.07	130.1	9.82	14.89	1.13	4.26	0.53	2.52	0.21	21.37	<0.02	<0.01
16*	2.98	14.56	0.45	294.20	0.13	0.13	<0.04	69.1	7.86	12.42	0.97	2.93	0.41	1.86	0.26	26.51	1.60	<0.02
<i>Mau-37 Crystal 1</i>																		
1	5.53	<28.26	13.87	419.34	0.31	0.20	<0.06	129.3	7.80	11.48	1.03	3.34	0.43	3.24	8.32	17.12	8.16	0.00
2	310.73	264.14	3.96	385.42	0.32	0.82	0.04	117.0	5.49	8.49	0.73	1.91	0.29	2.50	17.99	21.39	0.85	0.01
3	11.31	162.72	1.89	355.29	0.37	0.16	0.01	129.1	11.38	15.83	1.21	3.63	0.34	2.37	10.71	24.47	0.35	0.01
4	923.47	235.12	35.62	948.61	7.32	1.62	0.64	2352.1	13.50	26.84	2.64	9.79	1.92	4.45	9.89	31.53	1.14	0.11
6	112.98	64.45	9.49	416.81	0.34	1.01	0.09	198.9	7.42	11.23	0.92	2.82	0.36	2.61	2.97	24.97	1.05	0.02
10*	40.19	25.91	0.96	394.33	0.40	0.32	<0.06	145.8	5.81	9.89	0.76	2.97	0.62	2.50	0.32	18.84	0.15	0.02

Point location is shown in Fig. 6.

*Spot diameter is 60 μm .

0.7080 and 0.7112 (Fig. 7). The thin rim has an even higher $^{87}\text{Sr}/^{86}\text{Sr}_i$ (0.7134). The plagioclase crystal from the outer enclave has a less radiogenic core and exhibits a slight increase towards the rim (0.7105 for core and \sim 0.7115 for rim). An increase to more radiogenic values is observed only for the overgrowth rim, where $^{87}\text{Sr}/^{86}\text{Sr}_i$ ratios are around 0.7130.

Crystal Mau39B-C3 from the contact zone shows an irregular zoning pattern with the An-poor zones exhibiting the most radiogenic Sr isotopic signature (0.7117–0.7123) whereas the An-rich rims have $^{87}\text{Sr}/^{86}\text{Sr}_i$ of 0.7108. Given the irregularity in the zoning pattern no distinct isotopic profile can be defined. Plagioclase from the host granite Mau-29 shows an isotopic profile with lower $^{87}\text{Sr}/^{86}\text{Sr}_i$ (0.7108) at the core and a rimward increase (0.7125–0.7129) to more radiogenic overgrowths (0.7130).

Compositional and isotopic co-variations

The variation in trace element composition appears to be positively correlated with $^{87}\text{Sr}/^{86}\text{Sr}_i$ for ΣLREE , Ba, and

Sr. This is especially evident for plagioclase crystals from samples Mau-26 and Mau37; high Sr isotopic ratios correlate with increased ΣLREE , Sr, and Ba contents. The opposite behavior is observed for Pb, which exhibits mirrored profiles in relation to the other trace elements. Important correlations are observed for Mau-26 as Eu and Sr contents follow the rimward decrease of $^{87}\text{Sr}/^{86}\text{Sr}_i$, the same behavior being exhibited by Eu in Mau-39B.

DISCUSSION

The role of diffusion

All analyzed plagioclase profiles show a decrease in $^{87}\text{Sr}/^{86}\text{Sr}_i$ from the outer core to the rim, the only exceptions being crystals from the double enclave Mau-39B, in which the profiles show either irregular distributed values or a rimward increase. We interpret the decrease in $^{87}\text{Sr}/^{86}\text{Sr}_i$ from the more An-rich core to the An-poor rim to indicate that the crystal cores grew in a hotter,

Table 6: Rb–Sr isotopic composition of spots in plagioclase xenocrysts from enclaves and host granite

Sample, point	Crystal	Position	$^{87}\text{Sr}/^{86}\text{Sr}$	1σ	$^{87}\text{Rb}/^{86}\text{Sr}$	$^{87}\text{Sr}/^{86}\text{Sr}_{588}$	1σ
<i>Mau-37A</i>							
1	1	rim	0.71034	0.00009	0.09572	0.70954	0.00010
2	1	core	0.71541	0.00025	0.10869	0.71451	0.00018
3	1	inter	0.71196	0.00013	0.01540	0.71183	0.00016
4	1	recrys	0.71109	0.00009	0.06590	0.71054	0.00010
5	2	rim	0.71149	0.00013	0.12228	0.71047	0.00012
6	2	core	0.71258	0.00017	0.12928	0.71150	0.00015
7	2	rim	0.71674	0.00035	0.54445	0.71221	0.00013
8	2	recrys	0.71163	0.00012	0.06911	0.71105	0.00069
9	2	rim	0.71184	0.00012	0.09059	0.71009	0.00012
37_1	Matrix	core	0.71319	0.00001	0.46145	0.70940	0.00011
<i>Mau-26</i>							
1	2	rim	0.71262	0.00015	0.03583	0.71233	0.00013
2	2	core	0.71399	0.00010	0.05491	0.71354	0.00010
3	2	inter	0.71281	0.00012	0.01607	0.71268	0.00012
4	2	core	0.71327	0.00009	0.01914	0.71311	0.00010
5	2	inter	0.71197	0.00008	0.01370	0.71186	0.00008
7	3	rim	0.71074	0.00012	0.00247	0.71072	0.00012
8	3	inter	0.71205	0.00009	0.01611	0.71192	0.00009
9	3	core	0.71269	0.00017	0.02034	0.71252	0.00013
10	3	inter	0.71232	0.00011	0.01172	0.71222	0.00011
11	3	rim	0.71056	0.00009	0.02095	0.71039	0.00010
12	3	rim	0.71191	0.00012	0.01548	0.71178	0.00012
13	1	rim	0.71122	0.00018	0.00680	0.71116	0.00016
14	1	inter	0.71381	0.00013	0.02367	0.71362	0.00017
15	1	core	0.71695	0.00037	0.25506	0.71486	0.00068
16	1	inter	0.71174	0.00010	0.02359	0.71155	0.00011
17	1	core	0.71415	0.00022	0.04171	0.71381	0.00017
18	1	core	0.71206	0.00011	0.03569	0.71177	0.00013
19	1	inter	0.71067	0.00012	0.02539	0.71046	0.00013
20	1	rim	0.71443	0.00020	0.30473	0.71193	0.00019
22	1	recrys	0.71446	0.00019	0.07259	0.71386	0.00015
23	1	core	0.71413	0.00016	0.28202	0.71177	0.00025
26_1	Matrix_1	core	0.71249	0.00019	0.31410	0.70985	0.00014
26_2	Matrix_2	core	0.71109	0.00008	0.06722	0.71054	0.00012
<i>Mau-39B</i>							
1	1	rim	0.71398	0.00034	0.11833	0.71301	0.00025
2	1	inter	0.71162	0.00016	0.02034	0.71145	0.00014
3	1	core	0.71168	0.00011	0.01932	0.71152	0.00012
4	1	rim	0.71395	0.00024	0.09009	0.71321	0.00035
V3_2	1	inter	0.71369	0.00012	0.30248	0.71115	0.00013
V3_3	1	core	0.71610	0.00019	0.66493	0.71052	0.00014
5	3	rim	0.71579	0.00017	0.24650	0.71377	0.00019
6	3	core	0.71240	0.00014	0.02275	0.71221	0.00014
12	3	rim	0.71633	0.00028	0.59028	0.71138	0.00028
13	3	rim	0.72159	0.00027	1.54982	0.70860	0.00028
14	3	core	0.71733	0.00019	0.73480	0.71117	0.00015
7	2	rim	0.71354	0.00014	0.04098	0.71320	0.00010
8	2	core	0.71318	0.00009	0.02872	0.71294	0.00012
9	2	rim	0.71357	0.00012	0.01527	0.71344	0.00014
10	2	core	0.71922	0.00033	0.88380	0.71181	0.00025
11	2	core	0.71834	0.00044	1.20679	0.70822	0.00032
39_1	Matrix		0.71341	0.00007	0.34202	0.71060	0.00010
<i>Mau 29 host granite</i>							
1	1	core	0.71089	0.0002	0.01239	0.71079	0.00018
2	1	rim	0.71306	0.00009	0.02472	0.71286	0.00010
3	1	inter	0.71264	0.00011	0.01343	0.71253	0.00001

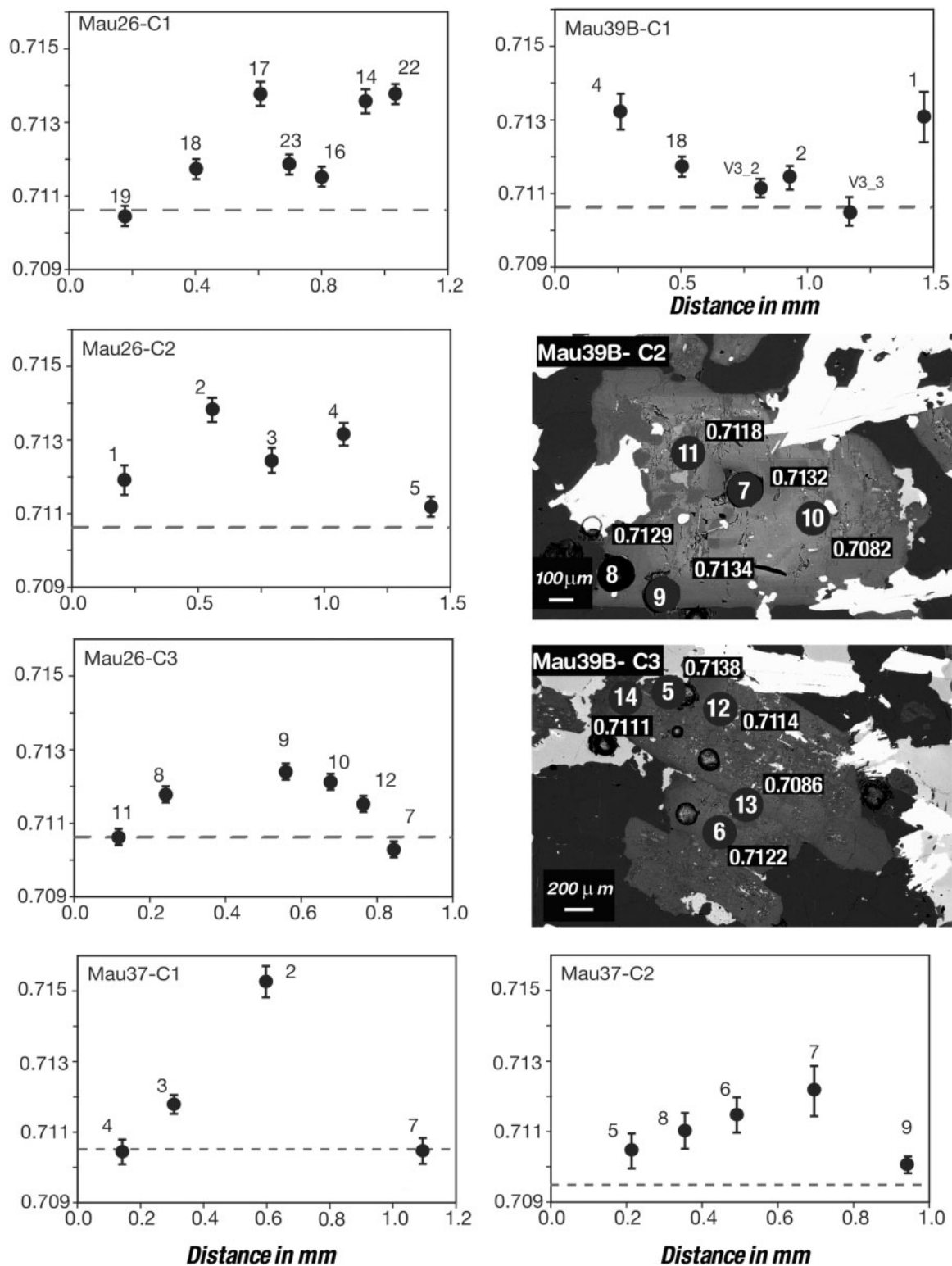


Fig. 7. Rim-to-rim Sr isotopic profiles (initial values) for plagioclase crystals compared with groundmass values (grey dashed lines). Error bars are 2 SD. Point locations are shown in Fig. 6. For crystals 2 and 3 from Mau-39B BSE images are shown, as no profiles can be drawn.

host-rock contaminated magma followed by one of the following: (1) crystallization in a progressively less radiogenic environment reflecting incremental replenishment of the magma chamber; (2) second-stage growth after isolation of the main body of the crystal-poor magma from the host-rock contaminant; or (3) near-solidus diffusion re-equilibration.

The third process is essentially solid state and because it can overprint any of the other two it must be considered first. In the discussion below we evaluate whether the progressive decrease in $^{87}\text{Sr}/^{86}\text{Sr}_i$ is a product of diffusive equilibration in an attempt to smooth the original compositional gradients between the more radiogenic cores and a more primitive enclave parental magma. The role of diffusion can be assessed using experimental data on diffusion coefficients (D_f to avoid confusion with D , meaning partition coefficients) and analytical solutions for diffusion from Fick's Second Law.

Sr diffusivity in plagioclase is a function of anorthite content and temperature (Giletti & Casserly, 1994). For the temperature we chose 810°C, which is the average zircon-saturation temperature (Watson & Harrison, 1983) of our rocks. Because the plagioclase rims show no substantial variation in An content we used average values for each crystal, for which a typical diffusion constant was estimated at $3.15 \times 10^{-15} \text{ cm}^2/\text{s}$. The resultant diffusion profiles are shown in Fig. 8. These profiles would require residence times varying from 8 to 31 kyr (considering the $^{87}\text{Sr}/^{86}\text{Sr}_i$ uncertainties) for Mau-26 crystals. Mau37-C2 data yield a notably smaller residence time under 6 kyr.

The significant variations in $^{87}\text{Sr}/^{86}\text{Sr}_i$ occur over relatively small distances. This is more evident in Mau37-C2 with $\Delta^{87}\text{Sr}/^{86}\text{Sr}_i$ (the absolute difference observed between core and rim values) of ~ 0.005 over a 60 μm distance. Davidson *et al.* (2001), in a study of plagioclase crystals from El Chichón, considered that isotopic changes $\Delta^{87}\text{Sr}/^{86}\text{Sr}$ of ~ 0.0008 over 300 μm are too punctuated to be attributable to diffusional re-equilibration, given that they were accompanied by changes in An content and dissolution textures. In this study, all the analyzed plagioclase crystals show intermediate Sr isotopic values that could be the product of diffusion and therefore the process cannot be dismissed as a potential cause of the isotopic profiles.

A Ba diffusion profile was determined for Mau26-C1 using the approach of Cherniak (2002) for oligoclase. The resultant diffusion coefficient at 810°C ($4.13 \times 10^{-18} \text{ cm}^2/\text{s}$) would require a residence time of between 1 and 7 Myr to account for the outer core-to-rim Ba decrease (Fig. 8). Among the REE, Nd is the only element with well-established diffusion data for oligoclase (Cherniak, 2003); a value of $2.56 \times 10^{-20} \text{ cm}^2/\text{s}$ was calculated at the same temperature. Using this diffusion coefficient, the profile in Mau26-C1 would require a residence time between 1 and

7 Myr, precluding the attribution of the Nd profiles to diffusion processes.

In conclusion, the profiles of trace elements with lower D_f values, such as Ba and REE, cannot have formed by diffusion, whereas the Sr isotope profiles could either be produced by diffusion or result from plagioclase growth from a host melt that is becoming progressively less radiogenic with time.

The significance of isotopic variation

More radiogenic cores: growth from a contaminated crystallization front

Cores and outer cores are the most radiogenic zones in all analyzed plagioclase crystals and have the highest An contents. Boxy plagioclase cores are observed in Mau-37 and the inner enclave of Mau-39B. Such a texture is attributed to fast growth rates in magmas usually undergoing mixing, with changes in magma chemistry combined with an elevation in temperature (Landi *et al.*, 2004), or to supersaturation as a result of metasediment assimilation (Castro, 2001). Given the highly radiogenic Sr isotopic signatures, we believe that the zoning textures we observe in xenocryst cores record early assimilation of radiogenic Sr from the wall-rocks, followed by filling of the partially resorbed plagioclase by re-equilibrated melts. The hypothesis is corroborated by isotopic heterogeneities observed in the inner enclave of Mau-39B, as patches with variable An content register different isotopic signatures. The biotite-rich, sheet-like enclaves, which are commonly associated with the fine, represent potential wall-rock contaminants in the melt, as also suggested by the $^{87}\text{Sr}/^{86}\text{Sr}$ ratio of 0.7140 calculated at 590 Ma for sample Mau-37A. Crystals 1 and 2 from Mau-26 show an increase in $^{87}\text{Sr}/^{86}\text{Sr}_i$ from core to outer core. Knesel *et al.* (1999) observed similar Sr isotopic profiles in sanidine crystals from the Taylor Creek Rhyolite, New Mexico; as these were not accompanied by an increase in total Sr content, the profiles were not attributed to an increase in the degree of melt contamination by the surrounding wall-rocks. In the Mauá case both crystals from sample Mau-26 record a Sr isotopic increase from the core to outer core coupled with higher trace elements contents, which is consistent with more extensive contamination.

More primitive rims: second-stage growth

Because the trace element zoning profiles illustrated in Fig. 6 cannot be explained by diffusional re-equilibration, we have to envisage a process capable of producing both isotopic and trace element zoning in the plagioclase rims. The rimward depletion in trace element abundance is inconsistent with the explanation that the Sr isotopic variations are attributable to growth through incremental replenishment by a new primitive magma invading the chamber. One would imagine that such a magma, from which little or no plagioclase had crystallized previously,

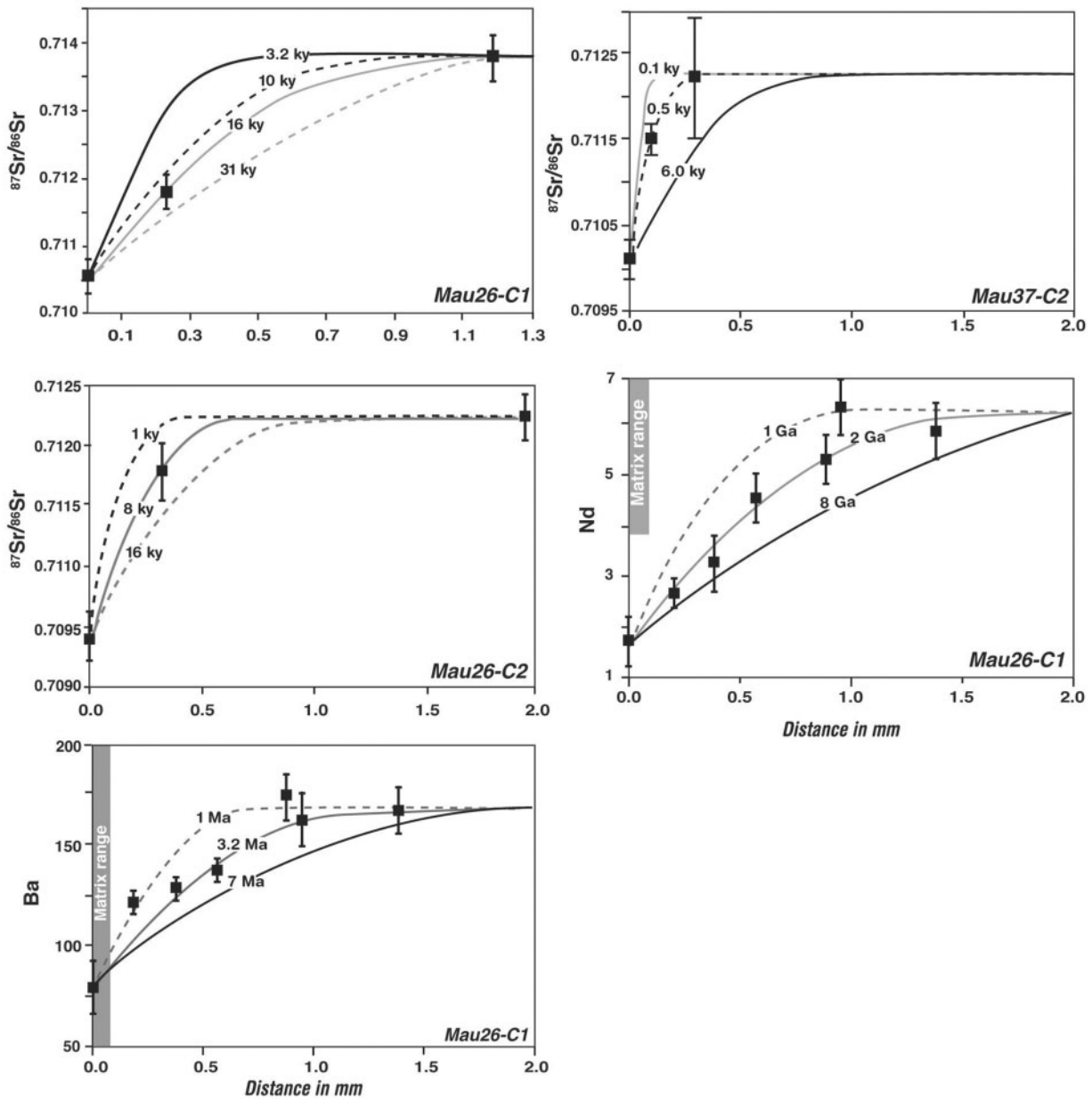


Fig. 8. Representative diffusion profiles for Sr, Ba and Nd for plagioclase crystals calculated using a mathematical solution for Ficks' Second Law of Diffusion.

would produce plagioclase that is more isotopically primitive and also richer in plagioclase-compatible trace elements, which is not observed. If incremental replenishment was to be considered viable, the recharging melt would have to be depleted in trace elements and the plagioclase crystals would finally be trapped by a melt with higher trace elements contents (as represented by the whole-rock composition of the enclaves, which shows a similar range to the host granites)—a scenario too complex and improbable. This leads us to three remaining hypotheses.

(1) *Growth in host granites.* As the enclaves and host granites have similar trace element compositions (except for Ba and Sr), plagioclase crystallizing from either magma would have similar trace element contents and profiles. Therefore, all crystallization could have taken place in the host granite, and the Sr isotopic decrease would then represent diffusional re-equilibration resulting from the entrapment of plagioclase by the enclave magma. Contrary to this is the observation that some of the plagioclase crystals from enclaves show zoning patterns indicative of disequilibrium (boxy and/or high-An cores

followed by normally zoned rims), which is not observed in any of the phenocrysts in the host granite. Moreover, phenocrysts from the representative host granite show an inverse isotopic profile, with less radiogenic cores and progressively more radiogenic rims.

(2) *Growth in a second stage after entrapment.* The xenocrystic cores are likely to have crystallized from a contaminated magma not directly related to the enclave parental magma, given that isotopic signatures from matrix crystals and whole-rock data are significantly less radiogenic than plagioclase cores. The decrease in trace element content in rims would be a result of post-entrapment crystallization from a more primitive melt (probably the enclave-forming magma) evolving by *in situ* fractional crystallization. For this to be possible growth rates would have to be fast enough to produce rims of significant size (over 500 μm in Mau26-C1) relative to the enclave matrix. Crystallization rates have been experimentally determined (Larsen, 2005) for resorbed anorthitic cores overgrown by more albitic rims, to investigate the effects on plagioclase growth during crystal transfer between basaltic and rhyodacitic magmas (i.e. with much more pronounced compositional differences than assumed here). Larsen (2005) demonstrated that growth rates can be as fast as 65×10^{-10} cm/s, with the resulting 100 μm rims formed in periods as short as 4 months. The core-to-rim decrease in the Sr isotopic initial ratios cannot be explained by the same mechanism, as isotopic fractionation is considered unrealistic at these magmatic conditions. Alternatively, intermediate isotopic profiles could reflect diffusion between the xenocrystic core and the newly formed rim. In this case, the residence time required to homogenize the isotopic signatures would be shorter, because the diffusion distance should consider homogenization through the half-distance between concentric spheres (Gagnevin *et al.*, 2005), and not between the outer core and the surrounding melt.

(3) *Growth after episodic contamination.* This hypothesis considers plagioclase crystallization from a melt in which assimilation is episodic and the contaminant/melt ratio is naturally and progressively decreased as a result of a sealing process in the crystallization front (Davidson *et al.*, 2007). The isotopic composition of the uncontaminated magma would have to be partly or nearly entirely recovered in the interstitial melts to produce the decrease in $^{87}\text{Sr}/^{86}\text{Sr}_i$ observed from outer cores to rims; that is, rims of plagioclase crystallizing under different contaminant/melt ratios should register progressively less radiogenic signatures; the core-to-rim decrease in trace element contents would reflect melt evolution by fractional crystallization.

The combined evaluation of textural features, trace element distribution and isotopic signatures permits hypothesis (1) (entrapment of former granite phenocrysts) to be ruled out. As for the remaining hypotheses [(2) and (3)], both are capable of explaining the chemical and isotopic

variations recorded in the plagioclase crystals. However, it is still necessary to explain crystals such as Mau39B-C1 with its less radiogenic core and more radiogenic rim. The crystal is in textural disequilibrium with the matrix and appears to be xenocrystic. A possible explanation would be formation of the core far from wall-rock contaminant surfaces and sinking to areas close to the chamber walls, resulting in inversion of the profile usually observed in the enclaves.

Significance of trace element profiles

If we consider a two-stage growth model, either post-contamination or post-entrapment, as responsible for the crystallization of the plagioclase rims then the trace element profiles would be the product of fractional crystallization and modeling of the process should be capable of reproducing the observed profiles. There is the possibility that intermediate values, in some cases, represent sampling of mixed domains in variable proportions during LA-Q-ICP-MS analysis. However, the fact that matrix crystals with no complex zoning show a similar range of values favors the hypothesis that the core-to-rim trace element decrease represents melt differentiation rather than a sampling artifact.

To test the effect of accessory minerals saturation on trace elements availability we calculated the LREE content of the melts in equilibrium with Mau26-C1, the plagioclase crystal with the most robust dataset. Partition coefficients (D) were calculated using the equations from Bédard (2006) at 810°C (zircon saturation temperature). The predicted concentrations are shown in Fig. 9a and compared with the whole-rock data. The melt compositions calculated for the cores are the closest to the whole-rock contents, which is consistent with the hypothesis that core crystallization, and therefore contamination, took place at higher temperatures, probably prior to melt saturation in accessory phases, probably allanite and apatite as well as zircon. D values from Mahood & Hildreth (1983) and Prowatke & Klemme (2006) were used to calculate the effect of allanite and apatite fractionation on the LREE content of the magma; zircon was ignored because of its low D values. The results indicate that fractionation of between 0.001 and 0.003% allanite and apatite could account for the core-to-rim La and Ce depletion. For Sm and Nd higher D values are required to attain the same results; this might be due to an increase of the partition coefficients for these elements in peraluminous systems (Bea *et al.*, 1994). More important is the observation that fractionation of minute amounts of accessory minerals can produce the observed LREE depletion, confirming that fractional crystallization plays the major role in controlling plagioclase trace element abundances.

Simulation of the fractionation of the total mineral assemblage requires a more complex model, given the number of partition coefficients involved. Hence the

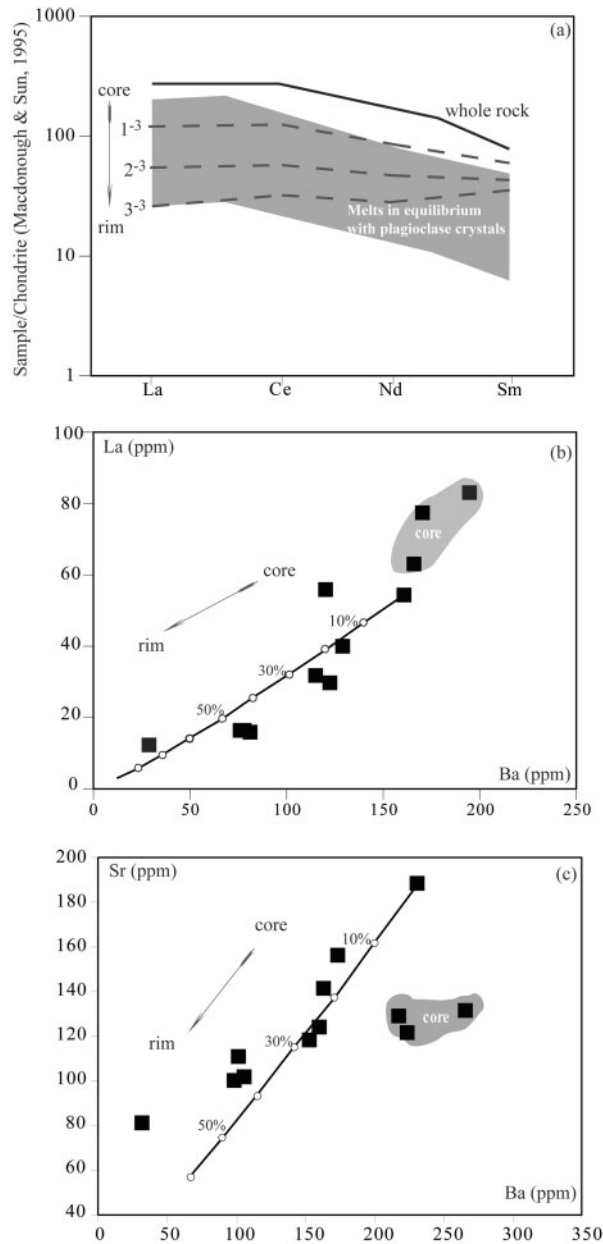


Fig. 9. (a) Results for allanite and apatite fractionation (dashed lines) calculated using trace element abundances in melts in equilibrium with analyzed plagioclase crystals (shaded area) and partition coefficients from Mahood & Hildreth (1983) and Provatke & Klemme (2006). (b) Ba vs La and (c) Ba vs Sr contents in melts in equilibrium with analyzed plagioclase crystals from sample Mau-26 and a fractionation model calculated using bulk partition coefficients (see Table 7 for D values). Intervals (circles) represent 10% fractionation; grey fields are core compositions.

models presented here are just an approximation to evaluate the influence of the removal of the major phases. Table 7 summarizes the D values used; the Sr value used is from Ren (2003), as the equations of Blundy & Wood

Table 7. Mineral partition coefficients used for calculation of melts in equilibrium with Mau26-C2

	D values				
	FK	plg	bt	all	ap
Ba	4*	0.7	3 [‡]		0.18**
La	0.07 [†]	0.4	2.59 [‡]	2300 [‡]	19.7**
Ce	0.03 [‡]	0.3		2060 [‡]	20.2**
Sr	2 [§]	3.5*	0.64 [†]	0.78 [§]	4.59**
Sm	0.02 [‡]	0.14		756 [‡]	28.3**
Nd	0.02 [‡]	0.21	0.9 [†]	1400 [‡]	57**
Pb	2.1 [§]	1.26		0.53 [§]	2.1**

*Ren (2003).

[†]Nash & Crecraft (1985).

[‡]Mahood & Hildreth (1983).

[§]Ewart & Griffin (1994).

[¶]Bédard (2006).

^{||}Provatke & Klemme (2006).

FK, alkali feldspar.

(1991) and Bédard (2006) resulted in too high values ($D \sim 7$), implying extremely low melt Sr contents of around 40–60 ppm, even for the matrix crystals and the host granite. Such small Sr contents are observed only in muscovite–biotite granites from more differentiated facies. Overestimation of D would reflect the high CaO content in peraluminous systems in which Sr partition shows a less steep relationship with An content (Ren, 2003).

The regression line for Ba vs La, considering the first point after the outer cores as the starting composition, indicates fractionation of 40–50% from core to rim (Fig. 9b), increasing to 70% for rim+overgrowth. The regression for Ba vs Sr (Fig. 9c) has to be considered with caution given the uncertainties in D values noted above. However, the rim variation is consistent with the same range of fractional crystallization indicated by the previous regression: about 40% for the rim region, with the exception being one data point (>50%) that was sampled together with overgrowth material. Core values are clearly displaced to lower Ba values and this is most probably a response to the rise in partition coefficients as a result of higher An content.

The application of the models proposed here for Mau26-C1 to different enclave xenocrysts has to be carried out with caution as there is variation in the absolute values for different crystals, indicating that these nucleated and crystallized at different stages of magmatic evolution. Moreover, differences in whole-rock data (both elemental and isotopic) suggest the possibility of enclave formation

from magmas and under evolutionary processes that are not necessarily identical.

THE ORIGIN OF MICROGRANITIC ENCLAVES

In the Mauá Pluton the *fme* have the same mineralogy, chemical and isotopic signatures as their host granite. At the whole-rock scale such similarities have been alternatively attributed to effective mixing between compositionally contrasted magmas (Castro *et al.*, 1990), reworking of early crystallized chilled margins (Dodge & Kistler, 1990; Donaire *et al.*, 2005), or interaction between compositionally similar magmas (Wiebe & Adams, 1997; Holness *et al.*, 2005; Wiebe *et al.*, 2007).

The origin of felsic enclaves through protracted hybridization between contrasting coeval magmas is not favored for the Mauá Pluton in view of the absence of any evidence for primitive magmas, both in the field and in the trace-element and Sr isotope signatures of the plagioclase xenocryst cores. We also consider it improbable that the predominant *fme* correspond to fragments of chilled margins or magma conduits, in view of the following features: (1) widespread distribution, not related to marginal portions of the pluton; (2) elliptical shapes in part with corrugated margins that locally mold around host-rock megacrysts; (3) the presence, in many *fme*, of alkali feldspar xenocrysts with sizes, shapes and often orientations similar to those of the host granite, indicating plastic behavior when the enclave melt was in contact with the host granitic mush. Evidence for solid rock fragments that sank in a granite mush seems to apply only to enclaves with angular shapes, such as the tabular biotitic enclaves and the scarce blocks of medium-grained equigranular granite.

In our view, interaction between compositionally similar magmas, a 'self-mixing' process, is the mechanism that best explains the structural, textural and compositional relationships of the *fme* in the Mauá Pluton. In such a model, two distinct origins have been proposed in the recent literature for the replenishing felsic melt that gives rise to the *fme*: lighter interstitial melts derived from an underlying layer of more primitive magma evolving by crystal fractionation (Holness *et al.*, 2005), or new batches of hotter and less dense felsic melt; for example, formed by reheating of the magma mush (Couch *et al.*, 2001; Wiebe *et al.*, 2007).

The model of Holness *et al.* (2005) is a two-stage process in which evolved melts derived from an underlying layer of hydrous, denser, more primitive magma could rise through the chamber as a response to the bulk density decrease of the interstitial melts caused by crystal fractionation (see also Stephen *et al.*, 1984). Other models also require the presence of more primitive magma, either as a

layer ponding at the base of the chamber (Couch *et al.*, 2001) or as a large dyke intruding the magma mush (Wiebe *et al.*, 2007).

Our preferred model for the generation of *fme* in the Mauá Pluton is analogous to that proposed by Holness *et al.* (2005) and considers the whole-rock chemistry of samples Mau-29 (host granite) and Mau-26 (most 'primitive' enclave) as representative of interacting liquids of very similar composition (Fig. 10). The curves were calculated using MELTS (Ghiorso & Sack, 1995) and represent the evolution of the system density for the host granites at different temperatures and water contents. A pressure of 3 kbar was estimated from the composition of primary muscovite crystals from an equigranular granite sample using the model of Massone & Schreyer (1987). Dashed lines in Fig. 10 represent the density of the enclave system at the onset of crystallization, taken as the zircon saturation temperature. Also shown are curves for the crystal cargo in the main chamber (25, 30 and 40%) and the field proposed as best for magma interaction. This field is delimited by the beginning of crystallization of both feldspars (as they occur as xenocrysts in the enclaves) and the attainment of rheological lockup, usually considered to be around 30% (see Petford, 2003). As an effect of crystallization in the chamber, a density contrast would exist even if the water content of the replenishment magma were the same as that of the magma filling the main chamber. The upward movement of the replenishing magmas would be possible if its entrance occurred after the density inversion (intersection between curves and lines). In this case, the formation of enclaves would be associated only with a temperature contrast, which could vary from 30 to 80°C inside the proposed interaction field and considering the same water content for both the resident and replenishing magmas.

CONCLUDING REMARKS

This study has combined *in situ* isotopic and trace element zoning in plagioclase xenocrysts from felsic microgranular enclaves to reveal a complex interplay of open-system processes involving wall-rock contamination, magma recharge and *in situ* evolution of both the enclave-forming magma and the host granite. Figure 11 summarizes the main conclusions and proposes a genetic model for the formation of felsic microgranular enclaves and the pipe-vortex encountered in the Mauá pluton.

Trace element profiles in plagioclase xenocrysts from enclaves can be reproduced by simulation of fractional crystallization using either the host-granite or the enclave whole-rock chemistry as the parental magma. Isotope profiles cannot be used to decipher whether the xenocryst rims grew within or outside the enclaves; that is, it is not possible to discern whether crystals were

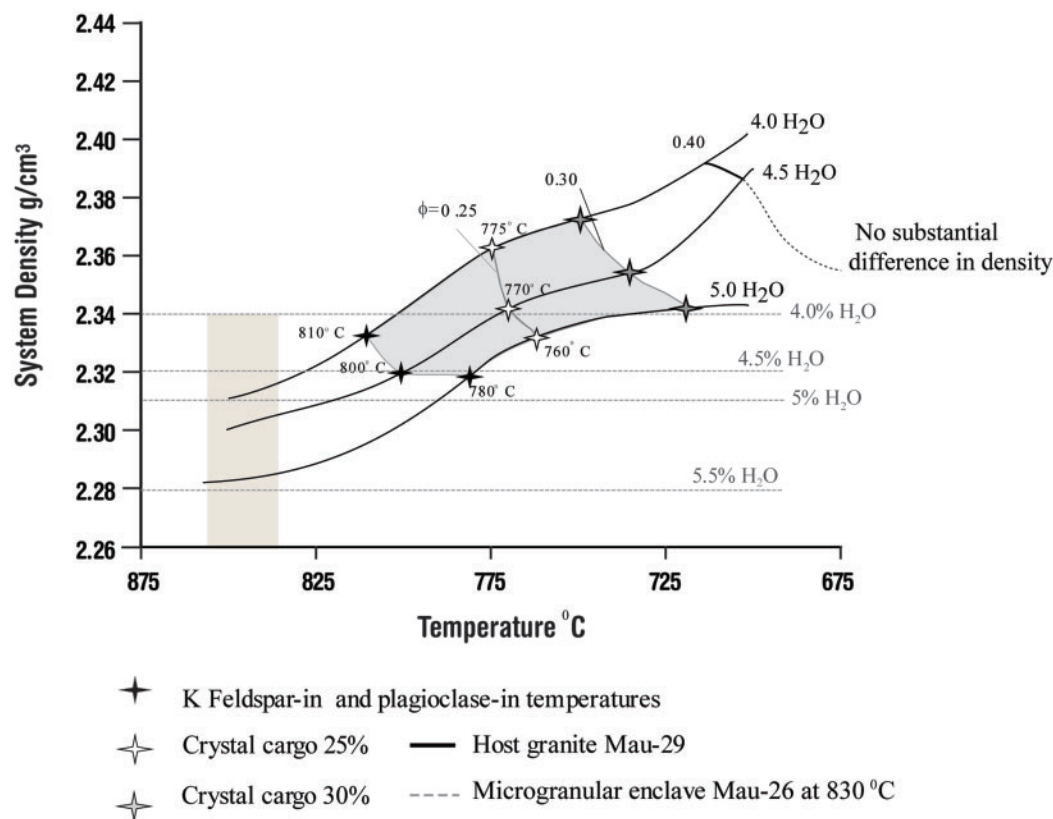


Fig. 10. Simulation of system density evolution using Mau-29 as representative of the chamber system at 3 kbar. Different curves calculated using variable water contents. Dashed lines represent the density of the enclave-forming magma (composition considered as that of Mau-26) under the same pressure and at the appropriate zircon saturation temperature (shaded area on the left of the diagram). Stars mark crystallization evolution at the onset of crystallization of both feldspars (in black) and attainment of crystal cargos (ϕ) of 25 and 30% (white and grey stars, respectively). The density of the most H₂O-rich melt composition is nearly stable after above 725°C. The grey shaded area marks the field considered suitable for convective mixing, taken as that between the feldspar-in temperature and attainment of rheological lock-up.

trapped after their complete crystallization in cumulate bands or if the rims crystallized from the enclave-forming magmas. In the hypothesis in which rim growth occurred after entrapment, the intermediate Sr isotope ratios could be due to diffusional equilibration, whereas trace elements register melt depletion by crystallization of the enclave-forming magma. On the other hand, if all crystallization proceeded in cumulate bands, there has to be an isolation of the contaminant as crystallization proceeds to permit isotopic ratios to be at least in part preserved.

One important aspect of our model is that the participation of more mafic magma is not required, neither as a precursor of the enclave-forming melts nor as heat source, and an autolithic origin is not supported by field and petrographic evidence. Therefore it can be argued that compositionally similar felsic magmas can mingle and produce microgranular enclaves in the ideal case where the replenishment magma injects into a chamber system that is already partially crystallized and therefore colder and denser.

ACKNOWLEDGEMENTS

This work was funded by FAPESP (grants 04/09942-0 and 07/00635-5). The authors are grateful to Marcos Mansueto and Sandra Andrade (Instituto de Geociências, Universidade de São Paulo) for their help with microprobe analyses and whole-rock major and trace elements analyses. Catherine Ginibre (Département de Minéralogie, Université de Genève) is also thanked for helpful guidelines regarding the best conditions for acquisition of back-scattering images. Lucelene Martins, Sebastian Tappe, Jason Cameron, Vivian Azor, and especially Judy Schultz are thanked for help throughout the analytical procedures. Detailed thoughtful reviews by Robert Wiebe, Charlotte Allen, an anonymous reviewer, and the editors Ron Frost and Marjorie Wilson helped to improve the manuscript.

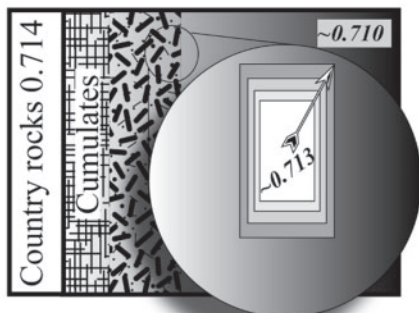
SUPPLEMENTARY DATA

Supplementary data for this paper are available at *Journal of Petrology* online.

Xenocryst formation

Scenario A

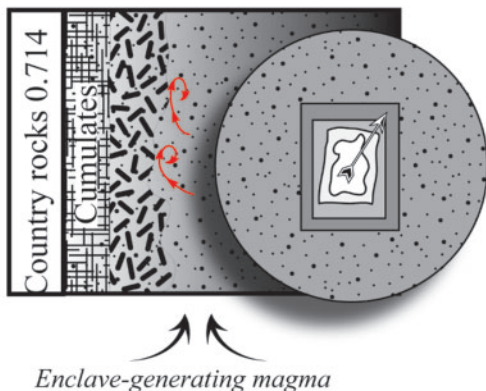
Isolation of contaminant by crystallization



Sealing of contaminant and recovery of isotope identity the magma, while it evolves by FC. Crystals are trapped by enclave-forming magma after complete crystallization.

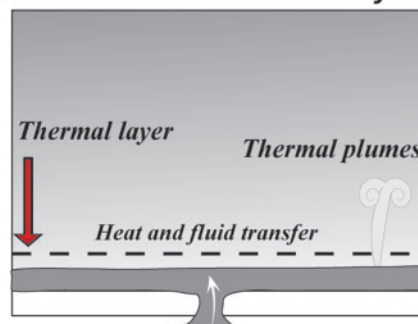
Scenario B

Disruption of cumulates



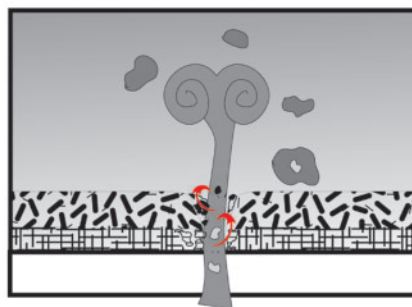
Cumulate disruption and incorporation of contaminated xenocrysts with partial dissolution and crystallization of rims registering FC of the enclave-forming magmas and diffusional reequilibration of Sr isotope ratio.

Before attainment of density contrast



The replenishing batch stabilises as a stratified layer at the bottom of the chamber and releases fluids and heat to the overlying magma triggering convection movements. The mechanism is probably an important part of the differentiation process.

After density contrast is attained



Replenishing batches immediately rise and might break and freeze in the form of microgranitoid enclaves.

Fig. 11. Schematic representation of xenocryst formation and the role played by replenishing magma batches in the Mauá chamber.

REFERENCES

- Bea, F., Pereira, M. D. & Stroh, A. (1994). Mineral/leucosome trace-element partitioning in a peraluminous migmatite (a laser ablation-ICP-MS study). *Chemical Geology* **117**, 291–312.
- Bédard, J. H. (2006). Trace element partitioning in plagioclase feldspar. *Geochimica et Cosmochimica Acta* **70**, 3717–3742.
- Bizzarro, M., Simonetti, A., Stevenson, R. K. & Kurszlauskis, S. (2003). *In situ* $^{87}\text{Sr}/^{86}\text{Sr}$ investigation of igneous apatites and carbonates using laser-ablation MC-ICP-MS. *Geochimica et Cosmochimica Acta* **67**, 289–302.
- Blundy, J. D. & Wood, B. J. (1991). Crystal-chemical controls on the partitioning of Sr and Ba between plagioclase feldspar silicate

- melts and hydrothermal solutions. *Geochimica et Cosmochimica Acta* **55**, 193–209.
- Browne, B. L., Eichelberger, J. C., Patino, L., Vogel, T. A., Dehn, J., Uto, K. & Hoshizumi, H. (2006). Generation of porphyritic and equigranular mafic enclaves during magma recharge events at Unzen Volcano, Japan. *Journal of Petrology* **47**, 301–328.
- Castro, A. (2001). Plagioclase morphologies in assimilation experiments. Implications for disequilibrium melting in the generation of granodiorite rocks. *Mineralogy and Petrology* **71**, 31–49.
- Castro, A., Moreno-Ventas, I. & De la Rosa, J. D. (1990). Microgranular enclaves as indicators of hybridization processes in granitoid rocks, Hercynian Belt, Spain. *Geological Journal* **25**, 391–404.
- Cherniak, D. J. (2002). Ba diffusion in plagioclase. *Geochimica et Cosmochimica Acta* **66**, 1641–1650.
- Cherniak, D. J. (2003). REE diffusion in feldspar. *Chemical Geology* **193**, 25–41.
- Collins, W. J., Wiebe, R. A., Healy, B. & Richards, S. W. (2006). Replenishment, crystal accumulation and floor aggradation in the megacrystic Kameruka Suite, Australia. *Journal of Petrology* **47**, 2073–2104.
- Costa, F., Dohmen, R. & Chakraborty, S. (2008). Time scales of magmatic processes from modeling zoning patterns of crystals. In: Rosso, J.J., Minerals, Inclusions and Volcanic Processes. *Mineralogical Society of America, Reviews in Mineralogy and Geochemistry* **69**, 545–594.
- Couch, S., Sparks, R. S. J. & Carroll, M. R. (2001). Mineral disequilibrium in lavas explained by convective self-mixing in open magma chambers. *Nature* **411**, 1037–1039.
- Davidson, J. P. & Tepley, F. J. (1997). Recharge in volcanic systems: Evidence from isotope profiles of phenocrysts. *Science* **275**, 826–829.
- Davidson, J., Tepley, F. J., Palacz, Z. & Meffan-Main, S. (2001). Magma recharge, contamination and residence times revealed by *in situ* laser ablation isotopic analysis of feldspar in volcanic rocks. *Earth and Planetary Science Letters* **184**, 427–442.
- Davidson, J. P., Morgan, D. J., Charlier, B. L. A., Harlou, R. & Hora, J. M. (2007). Microsampling and isotopic analysis of igneous rocks: Implications for the study of magmatic systems. *Annual Review of Earth and Planetary Sciences* **35**, 273–311.
- Didier, J. (1973). *Granites and their Enclaves*. New York: Elsevier, 393 pp.
- Didier, J. & Barbarin, B. (eds) (1991). *Enclaves and Granite Petrology. Developments in Petrology* **3**.
- Dodge, F. C. W. & Kistler, R. W. (1990). Some Additional observations on inclusions in the granitic rocks of the Sierra Nevada. *Journal of Geophysical Research* **17**, 841–848.
- Donaire, T., Pascual, E., Pin, C. & Duthou, J.-L. (2005). Microgranular enclaves as evidence of rapid cooling in granitoid rocks: the case of the Los Pedroches granodiorite, Iberian Massif, Spain. *Contributions to Mineralogy and Petrology* **149**, 247–265.
- Ewart, A. & Griffin, W. L. (1994). Application of proton-microprobe data to trace-element partitioning in volcanic rocks. *Chemical Geology* **117**, 251–284.
- Filipov, M. & Janasi, V. A. (2001). The Mauá granitic massif, Central Ribeira Belt, São Paulo: petrography, geochemistry and U–Pb dating. *Revista Brasileira de Geociências* **31**, 341–348.
- Frost, T. P. & Mahood, G. A. (1987). Field, chemical and physical constraints on mafic–felsic interaction in the Lamar Granodiorite, Sierra Nevada, California. *Geological Society of America Bulletin* **99**, 272–291.
- Gagnevin, D., Daly, J. S., Poli, G. & Morgan, D. (2005). Pb isotopic zoning of K-feldspar megacrysts determined by laser ablation multi-collector ICP-MS: Insights into granite petrogenesis. *Geochimica et Cosmochimica Acta* **69**, 1899–1915.
- Ghiorso, M. S. & Sack, R. O. (1995). Chemical mass transfer in magmatic processes. IV: A revised and internally consistent thermodynamic model for the interpolation of liquid–solid equilibria in magmatic systems at elevated temperatures and pressures. *Contributions to Mineralogy and Petrology* **119**, 197–212.
- Giletti, B. J. & Casserly, J. (1994). Strontium diffusion kinetics in plagioclase feldspars. *Geochimica et Cosmochimica Acta* **58**, 3785–3793.
- Holness, M. B., Martin, V. M. & Pyle, D. M. (2005). Information about open-system magma chambers derived from textures in magmatic enclaves: the Kameni Islands, Santorini, Greece. *Geological Magazine* **142**, 637–649.
- Janasi, V. A., Alves, A. & Vlach, S. R. F. (2003). Granitos peraluminosos da porção central da Faixa Ribeira, Estado de São Paulo: sucessivos eventos de reciclagem da crosta continental no neoproterozóico. *Geologia USP—Série Científica* **3**, 13–24.
- Knesel, K. M., Davidson, J. P. & Duffield, W. A. (1999). Evolution of silicic magma through assimilation and subsequent recharge: evidence from Sr isotopes in sanidine phenocrysts, Taylor Creek rhyolite, NM. *Journal of Petrology* **40**, 773–786.
- Landi, P., Métrich, N., Bertagnini, A. & Rosi, M. (2004). Dynamics of magma-mixing and degassing recorded in plagioclase at Stromboli (Aeolian Archipelago, Italy). *Contributions to Mineralogy and Petrology* **147**, 213–227.
- Larsen, J. F. (2005). Experimental study of plagioclase rim growth around anorthite seed crystals in rhyodacitic melt. *American Mineralogist* **90**, 417–427.
- Mahood, G. & Hildreth, W. (1983). Large partition coefficients for trace elements in high-silica rhyolites. *Geochimica et Cosmochimica Acta* **47**, 11–30.
- Massone, H. J. & Schreyer, W. (1987). Phengite geobarometry based on the limiting assemblage with K-feldspar, phlogopite, and quartz. *Contributions to Mineralogy and Petrology* **96**, 212–224.
- McDonough, W. F. & Sun, S.-s. (1995). The composition of the Earth. *Chemical Geology* **120**, 223–253.
- Nash, W. P. & Crecraft, H. R. (1985). Partition coefficients for trace elements in silicic magmas. *Geochimica et Cosmochimica Acta* **49**, 2309–2322.
- Paton, C., Woodhead, J. D., Hergt, J. M., Phillips, D. & Shee, S. (2007). Strontium isotope analysis of kimberlitic groundmass perovskite via LA-MC-ICP-MS. *Geostandards and Geoanalytical Research* **31**, 321–330.
- Petford, N. (2003). Rheology of granitic magmas during ascent and emplacement. *Annual Review of Earth and Planetary Sciences* **31**, 399–427.
- Pons, J., Barbey, P., Nachit, H. & Burg, J. P. (2006). Development of igneous layering during growth of pluton: The Tarçouate Laccolith (Morocco). *Tectonophysics* **413**, 271–286.
- Prowatke, S. & Klemme, S. (2006). Trace element partitioning between apatite and silicate melts. *Geochimica et Cosmochimica Acta* **70**, 4513–4527.
- Pupier, E., Barbey, P., Toplis, M. J. & Bussy, F. (2008). Igneous layering, fractional crystallization and growth of granitic plutons: the Dolbel Batholith in SW Niger. *Journal of Petrology* **49**, 1043–1068.
- Ramos, F. C., Wolf, J. A. & Töllstrup, D. L. (2004). Measuring ⁸⁷Sr/⁸⁶Sr variations in minerals and groundmass from basalts using LA-MC-ICPMS. *Chemical Geology* **211**, 135–158.
- Ren, M. (2003). Partitioning of Sr, Ba, Rb, Y, and LREE between plagioclase and peraluminous silicic magma. *American Mineralogist* **88**, 1091–1103.
- Schmidberger, S. S., Simonetti, A. & Francis, D. (2003). Small-scale Sr isotope investigation from peridotite xenoliths by laser ablation MC-ICP-MS—Implications for mantle metasomatism. *Chemical Geology* **199**, 317–329.

- Stephen, R., Sparks, J. & Huppert, H. E. (1984). Density changes during the fractional crystallization of basaltic magmas: fluid dynamic implications. *Contributions to Mineralogy and Petrology* **85**, 300–309.
- Theodorovicz, A., Yamato, A. A., Takahashi, A. T., Vasconcelos, C. S., Santarém, P. C. & Silva, V. A. (1992). *Projeto Santa Isabel, Mogi das Cruzes e Mauá. CPRM, promineiro, Portuguese, Final Report, 194*.
- Töbisch, O. T., McNulty, B. A. & Vernon, R. H. (1997). Microgranitoid enclave swarms in granitic plutons, central Sierra Nevada, California. *Lithos* **40**, 321–339.
- Vernon, R. H. (1984). Microgranitoid enclaves in granites—globules of hybrid magma quenched in a plutonic environment. *Nature* **309**, 438–439.
- Waight, T. E., Dean, A. A., Maas, R. & Nicholls, I. A. (2000). Sr and Nd isotopic investigations towards the origin of feldspar megacrysts in microgranular enclaves in two I-type plutons of the Lachlan Fold Belt, southeast Australia. *Australian Journal of Earth Sciences* **47**, 1105–1112.
- Waight, T. E., Maas, R. & Nicholls, I. A. (2001). Geochemical investigations of microgranitoid enclaves in the S-type Cowra Granodiorite, Lachlan Fold Belt, SE Australia. *Lithos* **56**, 165–186.
- Waight, T. E., Wiebe, R. A. & Krogstad, E. J. (2007). Isotopic evidence for multiple contributions to felsic magma chambers: Gouldsboro Granite, Coastal Maine. *Lithos* **93**, 234–247.
- Watson, E. B. & Harrison, M. (1983). Zircon saturation revisited: temperature and composition effects in a variety of crustal magma types. *Earth and Planetary Science Letters* **64**, 295–304.
- Weinberg, R. F., Sial, A. N. & Pessoa, R. R. (2001). Magma flow within the Tavares pluton, northeastern Brazil: Compositional and thermal convection. *Geological Society of America Bulletin* **113**, 508–520.
- Wiebe, R. A. (1974). Coexisting intermediate and basic magmas, Ingonish, Cape Breton Island. *Journal of Geology* **82**, 74–87.
- Wiebe, R. A. & Adams, S. D. (1997). Felsic enclave swarms in the Gouldsboro Granite, Coastal Maine: A record of eruption through the roof of a silicic magma chamber. *Journal of Geology* **105**, 617–627.
- Wiebe, R. A., Wark, D. A. & Hawkins, D. P. (2007). Insights from quartz cathodoluminescence zoning into crystallization of the Vinalhaven granite, coastal Maine. *Contributions to Mineralogy and Petrology* **154**, 439–453.